Plasma Sources
Science and
Technology

PAPER • **OPEN ACCESS**

On the plasma chemistry of a cold atmospheric argon plasma jet with shielding gas device

To cite this article: Ansgar Schmidt-Bleker *et al* 2016 *Plasma Sources Sci. Technol.* **25** 015005

OPEN ACCESS
IOP Publishing
Plasma Sources Science and Technology
Plasma Sources Sci. Technol. **25** (2016) 015005 (24pp)
doi:10.1088/0963-0252/25/1/015005

On the plasma chemistry of a cold atmospheric argon plasma jet with shielding gas device

Ansgar Schmidt-Bleker[1,2], Jörn Winter[1,2], André Bösel[2], Stephan Reuter[1,2] and Klaus-Dieter Weltmann[1]

[1] ZIK plasmatis, Felix-Hausdorff Str. 2, 17489 Greifswald, Germany
[2] INP Greifswald e.V., Felix-Hausdorff Str. 2, 17489 Greifswald, Germany

E-mail: ansgar.schmidt-bleker@inp-greifswald.de and stephan.reuter@inp-greifswald.de

Received 3 August 2015, revised 18 September 2015
Accepted for publication 2 October 2015
Published 10 December 2015

Abstract

A novel approach combining experimental and numerical methods for the study of reaction mechanisms in a cold atmospheric Ar plasma jet is introduced. The jet is operated with a shielding gas device that produces a gas curtain of defined composition around the plasma plume. The shielding gas composition is varied from pure N_2 to pure O_2.

The density of metastable argon $Ar(4s,^3P_2)$ in the plasma plume was quantified using laser atom absorption spectroscopy. The density of long-living reactive oxygen and nitrogen species (RONS), namely O_3, NO_2, NO, N_2O, N_2O_5 and H_2O_2, was quantified in the downstream region of the jet in a multipass cell using Fourier-transform infrared spectroscopy (FTIR).

The jet produces a turbulent flow field and features guided streamers propagating at several km s^{-1} that follow the chaotic argon flow pattern, yielding a plasma plume with steep spatial gradients and a time dependence on the ns scale while the downstream chemistry unfolds within several seconds. The fast and highly localized electron impact reactions in the guided streamer head and the slower gas phase reactions of neutrals occurring in the plasma plume and experimental apparatus are therefore represented in two separate kinetic models. The first electron impact reaction kinetics model is correlated to the LAAS measurements and shows that in the guided streamer head primary reactive oxygen and nitrogen species are dominantly generated from $Ar(4s,^3P_2)$. The second neutral species plug-flow model hence uses an $Ar(4s,^3P_2)$ source term as sole energy input and yields good agreement with the RONS measured by FTIR spectroscopy.

Keywords: plasma jet, plasma chemistry, Fourier-transform infrared spectroscopy, kinetic modeling, laser atom absorption spectroscopy, atmospheric pressure plasma

(Some figures may appear in colour only in the online journal)

1. Introduction

Cold atmospheric plasma (CAP) sources are of interest for their applicability in the field of plasma medicine. Several reviews on biomedical applications of CAP [1–4], the various kinds of CAP sources available [5–8] and the role of plasma generated reactive oxygen and nitrogen species (RONS) [9] can be found in the literature. An important goal in plasma medical research is to assign specific plasma-generated RONS (or specific RONS mixtures) to a given biological response. For this purpose shielding gas devices have previously been applied in order to control the environment of plasma jets and hence influence the RONS generated by the plasma [10, 11]. Continuously varying the shielding gas composition from pure

N_2 to pure O_2 then allows for the correlation of plasma generated species [12, 13] to biological effects such as viability [10], cytotoxicity and gene response of eukaryotes [14, 15] or antimicrobial effects [16]. Another approach is to use different operating modes of CAP sources to influence the species chemistry: Pavlovich *et al* have recently shown that nitrogen oxides-dominated plasma chemistry was more successful in bacterial inactivation than a plasma chemistry dominated by reactive oxygen species using different operating modes of a DBD [17], which is consistent with the findings of Jablonowski and Hänsch *et al* [16] obtained with the jet and shielding gas device employed in the present study.

The goal of this study is to investigate the reaction pathways that lead to the generation of RONS in an argon-operated CAP jet operated with a shielding gas device. Therefore, time-resolved measurements of the metastable state $Ar(4s,^3P_2)$ (in the following also denoted Ar^*) are performed in the plasma plume via laser atom absorption spectroscopy (LAAS) and the RONS O_3, NO_2, N_2O_5, N_2O, HNO_3 and H_2O_2 are monitored in the far-field of the jet using Fourier-transform infrared (FTIR) spectroscopy. While for biomedical applications, the long-living RONS in the far-field are merely of interest where safety issues are concerned (e.g. ensuring that RONS densities comply with threshold limit values), the RONS composition in the plasma plume of CAP jets differs significantly. In order to gain insight into the near-field RONS composition, two zero-dimensional reaction kinetics models are developed that describe the fast electron processes and the long-term kinetics of RONS separately. A parametric study is performed using shielding gas mixtures with varying composition and the models are correlated to data obtained from LAAS and FTIR measurements.

The approaches for numerical investigation of plasma processes in CAP jets operated with noble gases range from zero-dimensional kinetic models (also termed volume averaged) [18–21] to two dimensional self-consistent approaches [22–27]. While zero-dimensional models come with the advantage of short computation times, the resulting possibility of including thousands of chemical reactions and easy implementation, they naturally cannot be self-consistent and therefore require close correlation to experimental measurements and/or verification by space-resolved models. A major challenge in plasma chemistry modeling in CAP jets that feature guided streamers is that the relevant timescales range from nanoseconds (fast electron dynamics and propagation of guided streamers) to several milliseconds (gas phase reactions in the plasma plume of CAP jets) or in case of non-flow driven CAP sources (typically dielectric barrier discharges) even several seconds [19]. To overcome this problem, Naidis has developed a hybrid model [28, 29]: In a first step, the propagation of a single guided streamer is calculated, yielding the production rates of primary reactive species (such that are generated directly from electron impact reactions). The production rates are then used as input values for a zero-dimensional reaction kinetics model. A similar approach has recently been presented by Tian and Kushner [30], who have developed a 2D model that first computes the generation of primary species using the complete set of electron-impact reactions for one pulse. For the calculation of hundreds of subsequent pulses, the model reuses the previously computed generation rates, hence yielding much faster computation times than would be required for including the detailed electron model for every pulse.

In this work the argon-operated CAP jet kinpen is investigated by means of LAAS on the $Ar(4s,^3P_2)$ metastable state, FTIR spectroscopy and kinetic modeling. The CAP jet is operated at a frequency of $\sim$1 MHz with 3 slm pure argon as feed gas and a shielding gas device is employed with composition ranging from pure N_2 to pure O_2 at a flow rate of 5 slm. The quantification of RONS is experimentally challenging for two reasons: First, as no molecular admixtures are used, the RONS densities are comparably low. Second, at the given flow rate the Reynold number is $Re \approx 3000$ ($Re = v_0 d \nu^{-1}$, with kinematic viscosity $\nu = 1.5 \times 10^{-5}\ m^2\ s^{-1}$, average velocity $v_0 = 25\ m\ s^{-1}$ at nozzle outlet and nozzle diameter $d = 1.6$ mm) and hence the flow is fully turbulent. However, these operating parameters are of interest as they have been applied in several biological and medical studies using the kinpen 09 and the similar kinpen Med [14, 31–35]. The turbulence has also been verified experimentally by planar laser induced fluorescence (LIF) measurements on OH as tracer molecule [36] and Schlieren imaging [37]. Diagnostics on turbulent CAP jets is challenging as experimental techniques that rely on averaging procedures may give misleading results. An illustrative example is given in [38], where instantaneous snapshots of guided streamer emission are compared to phase resolved measurements (in which images with same phase respect to the voltage signal are averaged).

In a previous work it was found that in a similar argon-operated CAP jet (kinpen Sci), the guided streamer is following the argon channel in a turbulent jet flow. In helium-operated jets, it was recently found, that besides the lower required self-sustaining electric field in the helium channel, also an electrostatic focusing mechanism is responsible for the guidance of the streamer within the helium gas channel [37]. Phase resolved optical emission spectroscopy measurements suggest that the same mechanism may also be relevant for argon-operated jets [39]. Since the instantaneous densities of ambient species can be expected to be much lower than the averaged quantities obtained by molecular beam mass spectrometry and Reynolds-averaged computational fluid dynamics (CFD) simulations [40], the respective densities at the position of the guided streamer can be estimated to be between the value obtained for the laminar case [11] and the Reynolds-averaged values.

The kinetic model presented in this study is similar to the plug-flow models developed for argon-operated CAP jets by van Gaens and Bogaerts [21, 27, 41], in which the system of ordinary differential equations describing the reaction kinetics is solved together with an electron energy balance equation in a volume element co-moving with the flow and which has recently also been applied to study the kinpen operated with argon and molecular admixtures [27]. This work is an extension of our previous work where CFD simulations, kinetic modeling of gas phase reactions and FTIR spectroscopy was combined to investigate the RONS chemistry [12]. A highlight in the current work and an extension to previous

approaches is, that the different time- and length-scales are accounted for in this model using a novel approach involving two separate kinetic models: The first model accounts for the electron impact reactions that occur in a stationary volume element of 100 μm diameter in the streamer head. The Ar^* densities obtained in the model are fitted to experimental data using the time-dependent input power as a fitting parameter in the model. The model suggests, that Ar^* is the major reactive species, in the sense that other RONS are mainly generated from reactions of Ar^* with N_2, O_2 and H_2O. The second model hence uses an Ar^* source term as time-dependent energy input in a larger volume element of diameter 1 mm (corresponding to the diameter of the visible plasma plume). This model only accounts for neutral reactive species. The second model itself consists of three simulation steps accounting for (1) the reactions in the visible plasma plume, (2) the reactions in the far-field of the jet, where RONS are diluted due to diffusion and (3) reactions occurring in the multipass cell of the FTIR setup at reduced pressure. The RONS densities obtained from the second model are fitted to the densities obtained from FTIR spectroscopy using the magnitude of the Ar^* source term as fitting parameter. Compared to the models employed by Naidis [28, 29] and Tian and Kushner [30], which also treat fast electron impact processes and slower gas phase chemistry reactions in separate models, this approach comes with the advantage of fast computation times since here both models are zero-dimensional, allowing for vast parametric studies. The downside of this approach is, that it is not self-consistent and therefore requires close correlation to experimental data, here realized through LAAS and FTIR measurements.

2. Methods

2.1. Plasma jet and shielding gas device

In this study the cold atmospheric plasma jet kinpen 09 (neoplas tools, Germany) was used, which operates at a frequency of ~1 MHz [42]. The jet was operated with a shielding gas device producing an annular flow of a defined gas around the effluent of the plasma jet as described in [43]. As feed gas a flux of 3 slm argon corresponding to an average velocity of 25 m s^{-1} (ALPHAGAZ 1, Air Liquide, France), as shielding gas a mixture of nitrogen and oxygen (ibid.) at a flux of 5 slm (average velocity of 7 m s^{-1}) was applied. The visible effluent has a length of approximately 1 cm.

2.2. Laser absorption spectroscopy

Laser absorption spectroscopy was performed on the $Ar(1s_5 - 2p_9)$ optical transition at a wavelength of 811.53 nm using a novel acousto-optic laser system (EasyLAAS, neoplas control GmbH, Germany). The basic scheme of the laser system is similar to an external cavity diode laser in Littrow configuration. However, the frequency tuning is not realized by turning the grating but by altering the acoustic signal applied to the two included acousto-optic modulators (AOMs) [44, 45]. In consequence, fast single mode frequency tuning with a repetition frequency of 10 kHz at a tuning range of 30 GHz is achieved due to the lack of mechanically actuated elements. The maximum repetition rate is 50 kHz with 4.5 GHz tuning range. The here-presented measurements were performed at 1 kHz repetition rate and 30 GHz tuning range. By means of a single mode optical fiber, the laser radiation is transferred to the absorption setup. The collimated laser beam is reflected by an adjustable mirror and focused subsequently in the absorbing region of the plasma jet by an achromatic lens (focal length of 45 mm). A second achromatic lens collimates the beam before it enters an argon low pressure discharge lamp that acts as reference. Behind the reference lamp a band pass filter with a central wavelength of 810 nm and a full width at half maximum (FWHM) of 10 nm is utilized to block unwanted spectral components of the light emitted by the plasma jet. The intensity of the light is detected by a fast photodetector (HCA-S, Femto, Germany) providing a bandwidth of 200 MHz. In order to be able to conduct axially resolved measurements (z-direction), the plasma jet is precisely positioned by a motorized linear stage.

For temporally resolved measurements, the laser wavelength is kept at a constant value, which is adjusted to the maximum of the reference discharge absorption signal. The spectral absorption profile is determined by tuning the laser wavelength over the optical transition and averaging the transient signal. The respective frequency scaling is obtained by a Michelson interferometer included into the EasyLAAS AOM Laser system.

According to Lambert–Beers law the temporal optical density $\rho(\lambda, z, t)$ in axial direction is calculated from the absorption signal $I(\lambda, z, t)$ and the plasma-off signal I_0 by

$$\rho(\lambda, z, t) = -\ln \frac{I(\lambda, z, t)}{I_0(\lambda)} = \int_0^L k(\lambda, x, z, t)\mathrm{d}x \qquad (1)$$

where L is the absorption length, k is the absorption coefficient and x is the position in laser beam direction. The absorber density n is calculated by

$$n(x, z, t) = \frac{4\epsilon_0 mc^2}{e^2 \lambda_0 f P(\lambda)} \cdot k(\lambda, x, z, t), \qquad (2)$$

where ϵ_0 is the vacuum permitivity, m the electron mass, c the vacuum speed of light, e the elementary charge, λ_0 the center wavelength and f the oscillator strength of the transition. For the investigated $Ar(1s_5 - 2p_9)$ transition λ_0 and f are 811.5 nm and 0.457, respectively. Furthermore, the spectral absorber distribution is described by the normalized profile function $P(\lambda)$, where $\int_0^\infty P(\lambda)\mathrm{d}\lambda = 1$. The measured profile function is shown in figure 1 together with the best-fit Voigt profile. Due to the low gas temperature of the jet of about 330 K [37] and the operation at atmospheric pressure, Doppler broadening is small against the dominant pressure broadening. The Gaussian width of the Voigt profile is thus only 0.76 GHz, whereas the measured Lorentzian width is 12.8 GHz. The latter value is in good agreement with values determined by other groups in atmospheric pressure argon plasmas. In a filamentary argon discharge within a capillary, Schröter *et al* measured a Lorentzian width of 8.6 GHz [46]. Niermann *et al* found a Lorentzian width of 12.7 GHz

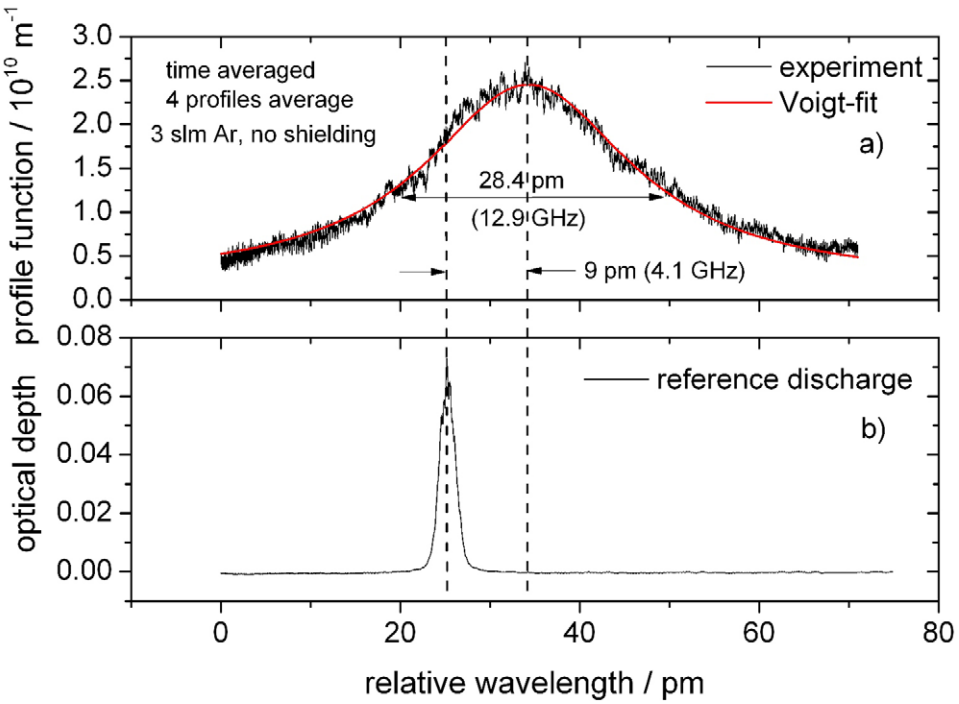

Figure 1. (a) absorption profile function measured on the plasma jet in the radial center and at the nozzle exit. The jet was operated with 3 slm Ar and no shielding gas. (b) absorption signal of the low pressure reference discharge.

from measurements on a parallel plate radio frequency driven μ-plasma jet operated in a mixture of He and Ar [47]. Besides the pressure broadening also a shift between the absorption maxima of the low pressure discharge and the plasma jet of about 9 pm (4.1 GHz) is observed.

Owing to the transient behavior of the filamentary plasma jet on a μs time scale, it is rather statistical whether a filament crosses the laser beam and generates a peak in the optical depth signal [47]. A straight forward evaluation and comparison of the temporal absorption signals at different axial positions and shielding gas settings is thus difficult. However, by recording the optical depth signal over a sufficient long time (4 ms in this work), a statistical analysis becomes possible. In this analysis, the 20 highest peaks of the optical depth are detected as exemplary shown in figure 2 for an axial position of $z = 2$ mm and a shielding gas composition of 1 slm $O_2 + 4$ slm N_2. In the further evaluation of different shielding gas compositions and axial positions, the average of those 20 peak values is used instead of a single absorption event.

The correct absorption length and argon metastable distribution within a single filament is unknown and therefore either an absorption length of the filament is assumed to estimate the argon metastable density (e.g. from emission measurements, as done in [48]) or just the line-of-sight density $\tilde{n}$ is given, which is calculated by

$$\tilde{n}(z,t) = \int_0^L n(x,z,t)\mathrm{d}x \frac{4\epsilon_0 mc^2}{e^2\lambda_0 f P(\lambda)} \cdot \rho(\lambda,z,t) \qquad (3)$$

From single shot emission measurements on a similar kinpen-type plasma jet over a single excitation period [38], the streamer width and therefore the absorption length is estimated to a value of about 100 μm. This value and the assumption of a homogeneous absorber distribution are used when comparing the simulated temporal argon metastable densities with the measurement.

2.3. FTIR absorption spectroscopy

In order to quantify RONS in the far field of the jet, FTIR absorption spectroscopy in the spectral range from 800 to 4000 cm^{-1} is used. A schematic of the experimental setup is shown in figure 3. The plasma jet with the shielding gas device is mounted to a glass chamber with a volume of 0.5 l. Both feed gas and shielding gas flux of the plasma jet are controlled using mass flow controllers (MFC, MKS Instruments, USA). In the acquired measurements the shielding gas composition was varied from pure nitrogen to pure oxygen. From the glass chamber, 4 slm of jet and shielding gas flow is sucked into a multipass cell (Bruker, USA) using a vacuum pump, while the rest of the gas exits the glass chamber through an exhaust pipe. The relative flux through the exhaust pipe was monitored using a ball flow meter. The MPC has a volume of around 15 l and provides an absorption length of $L = 32$ m. For the absorption measurements an FTIR spectrometer (Vertex 80v, Bruker, USA) was used. The pressure in the MPC was adjusted to 600 mbar. Prior to the experiments, the system was flushed with 3 slm Ar and 5 slm N_2 for 8 h in order to remove residual humidity from the system.

The identification and quantification of the reactive species was achieved using spectroscopic data from the HITRAN database and PNNL quantitative infrared database [49, 50]. The IR simulation software QMACSoft (neoplas control, Germany) was used to calculate cross sections from the molecular line data provided in the HITRAN database.

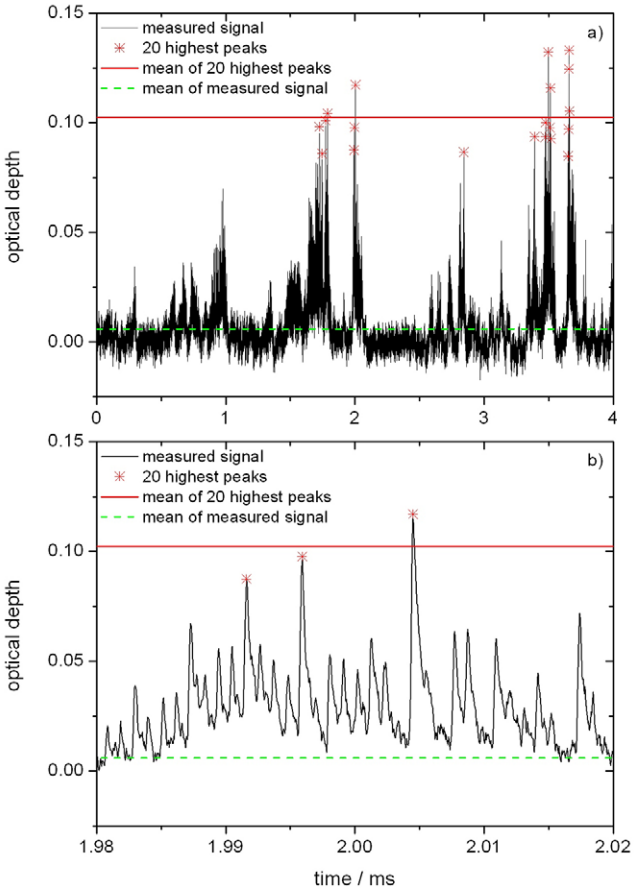

Figure 2. Temporal optical depth signal for a shielding gas setting of 1 slmO_2 + 4 slmN_2 at $z = 2$ mm. The symbols represent the 20 highest peaks and the solid horizontal line is the mean of those values. The mean value of the entire optical depth signal is represented by the dashed line. (b) is a closeup of (a).

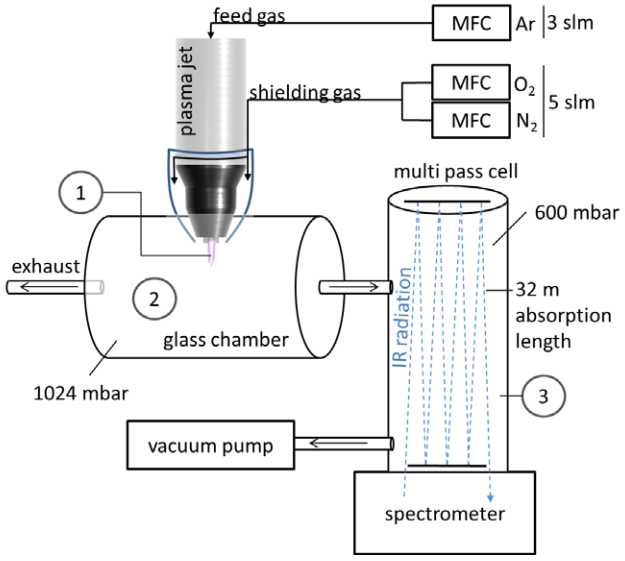

Figure 3. Schematics of the setup used in the FTIR measurements. The encircled labels 1–3 correspond to the simulation steps of the kinetic model as explained in the following section 2.4.

The densities n_i of the species $\{i\}$ were then used as a fitting parameter when fitting the absorbance function

$$A = -\ln\frac{I(\nu)}{I_0(\nu)} = \sum_i n_i \sigma_i(\nu) L \tag{4}$$

to the experimental data. Here I_0 is the background intensity measured when the plasma jet is turned off, ν is the wavenumber and σ_i are the respective cross sections. The intensity I_0 was acquired before the plasma jet was turned on with a shielding gas mixture of $n_{O_2}/n_{N_2} = 1$. In figure 4 the absorbance obtained from the experimental data and the respective fit is illustrated. The species O_3, NO_2, HNO_3, N_2O_5, N_2O, CO, and CO_2 could clearly be identified. An absorbance signal due to H_2O_2 was also fitted to the data, however as the signal is low and superposed by the N_2O_5 and HNO_3 signal, a clear identification is not possible as discussed in section 3.2.

In the previous work [12] a similar setup was used, however using an absorption length of 19.2 m and a MPC pressure of 100 mbar. These changes result in a tenfold higher sensitivity of the current system. However, using larger pressures in the MPC results in higher reaction rates, leading to the generation and destruction of reactive species in the MPC itself.

2.4. Numerical models

In the plasma plume, the energy is deposited through guided streamers, which typically feature high electric fields in the streamer head (single shot images of the streamer can be found in [38]). In the downstream region of the jet, the highly reactive species generated in these processes successively react to more stable compounds such as can be detected by FTIR spectroscopy. Two zero-dimensional kinetic models are developed in order to investigate both the fast electron impact reactions occurring locally in the head of the guided streamer and the slower reactive species chemistry occurring in the broader plasma plume and the measurement apparatus itself.

2.4.1. Electron impact plasma reaction kinetics model. The first kinetic model aims at investigating the generation of primary reactive species (such species that are generated directly from dissociation, electron attachment, ionization or excitation of N_2, O_2 or H_2O) through electron impact reactions in the streamer head at a fixed spatial position. Therefore, the system of ordinary differential equations describing the reaction kinetics,

$$\partial_t n_s = \sum_j \phi_{s,j} f_{s,j} R_j, \quad \text{with} \quad R_j = k_j \prod_i n_i^{f_{s,j}} \delta_{i,j} \tag{5}$$

is solved together with the electron energy balance equation

$$\partial_t\left(\frac{3}{2} n_e k_B T_e\right) = P_{in}(t) + \sum_j R_j \Delta\epsilon_j - \sum_j \frac{3}{2} R_j \left(\frac{2m_e}{M_j} k_B (T_e - T_g)\right). \tag{6}$$

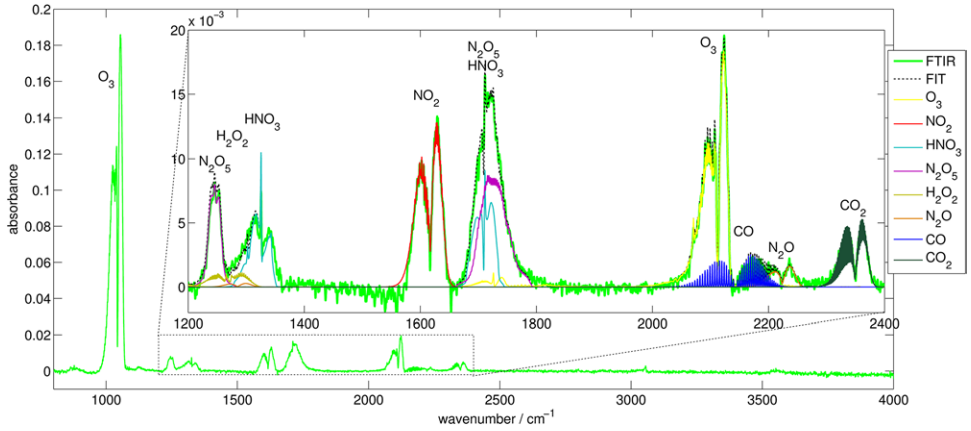

Figure 4. Absorbance as measured by FTIR spectroscopy and as obtained from the fitting procedure for individual species densities for a shielding gas composition of $O_2/N_2 = 0.2$.

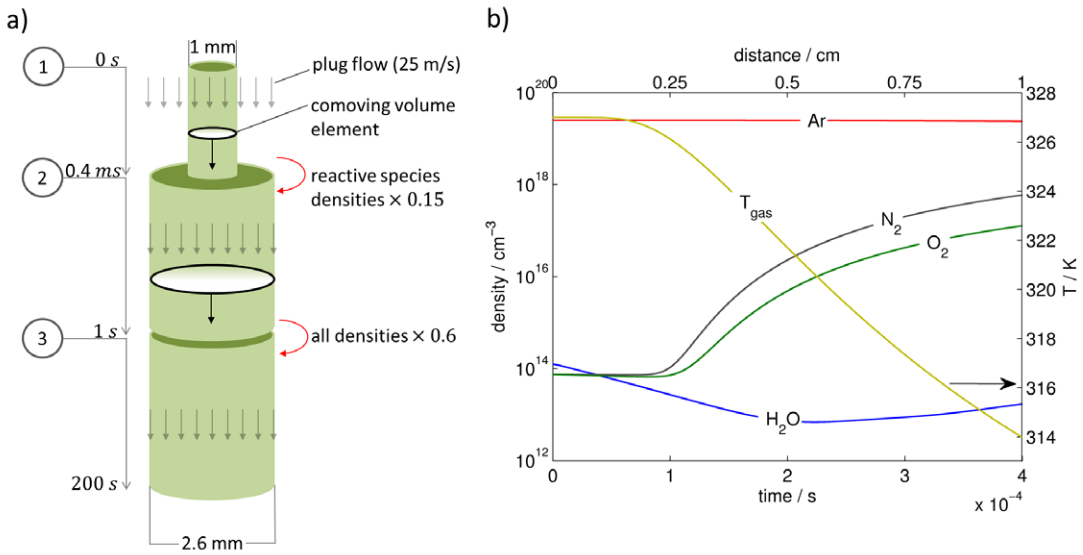

Figure 5. Illustration of the plug-flow approach used in the model (a) and densities of ambient species (shown for synthetic air shielding gas case), water impurities and gas temperature as assumed in the effluent model (b). The encircled labels 1–3 denote the simulation steps and can be identified with the corresponding labels in the experimental setup (figure 3).

Here R_j is the reaction rate of reaction j with the rate coefficient k_j, $\phi_{s,j}$ is 1 if species s is a product in reaction j and -1 if it is a reactant, $f_{s,j}$ is the stoichiometric number of species s in reaction j and $\delta_{i,j}$ is 1 if species i is a reactant in reaction j and 0 otherwise. In the energy balance equation T_e denotes the electron temperature (defined as $2/3\,k_B$ of the mean electron energy), k_B is the Boltzmann constant, $P_{in}(t)$ is the power transferred to the electrons, $\Delta\epsilon_j$ is the energy lost or gained in reaction j and M_j is the mass of the heavy species in reaction j. The last term is only evaluated for elastic collisions. The input power is defined as T-periodic Gaussian pulses

$$P_{in}(t) = \sum_m A \exp(-(t - (m + 1/2)T)^2/\tau^2) \qquad (7)$$

with $m \in \mathbb{N}$. The amplitude A and pulse width τ are chosen to match the excitation of Ar(4s,^{3}P$_2$) measured in the absorption measurements. The list of reactions E1 to E48 used in the electron impact model is given in table A1 in the appendix. Besides to electron impact reactions further quenching and radiative processes for the argon states are considered (reactions E9 to E23). Additionally, quenching of argon states by O_2, N_2 and H_2O as listed in table A2 (reactions R4-7 and R14-17) is considered.

2.4.2. Neutral reactive species reaction kinetics model. The electron impact plasma reaction kinetics model introduced in the previous section is designed for describing the fast and highly localized processes in the guided streamer head with an estimated width of 100 μm. For the investigation of reaction pathways of neutral RONS produced in the broader (diameter approximately 1 mm) plasma plume, a zero-dimensional (volume-averaged) plug-flow model is developed. As detailed in the below section 3.1, the Ar* density measurements and the electron impact model show that metastable argon is mainly responsible for the generation of primary reactive species. The neutral chemistry model hence uses an argon metastable source term as its sole energy input. The principle of the model is illustrated in figure 5 and will be described in the following. Only the reaction kinetics equations

$$\partial_t n_s = \sum_j \sigma_{s,j} f_{s,j} R_j + G_s(t), \quad \text{with} \quad R_j = k_j \prod_i n_i^{f_{s,j}\delta_{i,j}} \tag{8}$$

are solved for all reactive species in a volume element co-moving with the flow. Comparing to the balance equation for the electron impact model, the source term $G_s(t)$ is added. For N_2 and O_2 the source term

$$G_s(t) = n_s^{\max} \partial_t \exp(-r_0^2 v_0/(4Dz(t))) \tag{9}$$

describes the diffusion of shielding gas species into the active plasma. Equation (9) describes a typical on-axis density profile for ambient species diffusing into laminar jets [11]. Here $n_s^{\max}$ is the maximum density that species s reaches, r_0 the jet radius and D is the diffusion coefficient. However, it needs to be accounted for that the jet is operated in a turbulent flow regime. The temporally averaged diffusion of ambient species in this turbulent jet has been quantified in [40] using mass spectrometry measurements and Reynolds averaged CFD simulations. As the guided streamer follows the turbulent argon-air boundary [36], which is static on the timescale of streamer propagation (less than 0.5 μs), the local and instantaneous shielding gas density that the guided streamer sees is expected to be lower than the previously obtained average quantities. In the kinetic model the estimated value $D = 1\ \mathrm{cm^2\ s^{-1}}$ is chosen, which is five times higher than the standard value expected for molecular diffusion of air in argon, accounting for the increased mixing in the turbulent flow, but is still approximately only half of the value obtained in Reynolds averaged CFD models and mass spectrometry measurements. The influence of the diffusion coefficient on the generation of RONS is discussed in the appendix B. The volume element is assumed to move with a constant velocity of $v_0 = 25\ \mathrm{m\ s^{-1}}$, corresponding to the average gas velocity at the nozzle of the plasma jet. $z(t) = v_0 t$ is the position of the volume element. The reactive species accounted for in the model are Ar*, $Ar_2^*(Ar_2(a^3\Sigma_u^+))$, O, $O^*(O(^1D))$, $O_2^*(O_2(^1\Delta_g))$, O_3, N, $N_2^*(N_2(A^3\Sigma_u^+))$, NO, NO_2, N_2O, NO_3, N_2O_5, H, H_2, OH, H_2O, H_2O_2, HO_2, HNO, HNO_2, HNO_3. The set of reactions used in the model is given in table A2 in the appendix A.

The simulation is subdivided into three steps corresponding to the conditions in the experimental setup. The simulation steps successively model the reaction kinetics in the effluent, the glass chamber and the MPC as illustrated in figure 5(a):

Step 1: Plasma plume (0–0.4 ms). The diameter of the co-moving volume element is chosen as 1 mm in the plasma plume, which roughly corresponds to the diameter of the visible plume. This value is larger than the diameter of the guided streamer (estimated around 100 μm). The model can hence only yield densities averaged over the volume element, while the actual local densities may be higher or lower (due to diffusion). In the plasma plume region the T-periodic Ar* source term

$$G_{\mathrm{Ar}^*} = \sum_m G_{\max} \exp(-(t - (m + 1/2)T)^2/\tau^2) \tag{10}$$

is added, where $G_{\max}$ is the maximum production rate. For Ar* no further generation processes are included as it is the species carrying the highest energy in the model and hence an back-transfer of energy from other excited species is not expected. In figure 5(b) the density of N_2 and O_2 diffusing into the effluent of the jet, the feed gas Ar and H_2O originating from impurities in the gas bottles and/or tubing is shown. Also the temperature profile used in the model is given. The H_2O impurity density is not constant as H_2O is partially consumed. The temperature profile was chosen to agree with measurements obtained using a quantitative Schlieren technique as described in [51].

Step 2: Glass chamber (0.4 ms–1 s). In the second step the reaction kinetics in the glass chamber is modeled. As the argon jet will rapidly mix with the shielding gas in the turbulent flow, an instant dilution of all reactive species is assumed. In a plug flow this corresponds to an expansion of the volume element from 1 mm to 2.6 mm diameter (which at an average velocity of $25\ \mathrm{m\ s^{-1}}$ yields the total mass flow of 8 slm) and a dilution of the species by a factor 0.15. Based on previous computational fluid dynamics simulations of the flow field in the glass chamber, an average residence time of 1 s is assumed [12].

Step 3: Multi pass cell (1–200 s). In the MPC the pressure is reduced to 600 mbar and hence all species are diluted by a factor 0.6. The simulation is run up to a time of 200 s. However, as the reactive species are continuously measured while residing in the MPC, the densities computed by the model are averaged over the interval from $t = 1$ s to $t_{\max} = 120$ s. The maximum evaluation time $t_{\max}$ is chosen to give best agreement with the experimental values. Estimating $t_{\max}$ based on the flow rate of 4 slm through the MPC with a volume of 15 l at 600 mbar gives a residence time of 135 s which agrees reasonably well.

The average computation time for the all model steps and post processing routines on an Intel Xeon X5680 is 3.7 s enabling its application in vast parametric sweeps and in fitting routines.

3. Results and discussion

3.1. Density of Ar*

In figure 6 the average line-of-sight Ar* density of the 20 largest absorption peaks is shown at different axial positions and for shielding gas compositions ranging from pure N_2 to pure O_2. The general trend is that the average density is not substantially affected by the shielding gas composition. As the excitation of Ar* by the guided streamer occurs much faster than the quenching by molecular species, this implies that the local electric field provided in a single guided streamer head is not significantly affected by the shielding gas composition. However, at a distance of $z = 2$ mm the measured Ar* density is significantly lower for pure N_2 shielding gas, than when O_2 is present. For the kinpen operated with He feed gas it was found that O_2 in the shielding gas significantly promotes the propagation of the guided streamer through an electrostatic focusing mechanism caused by anions (e.g. O_2^-, O^-) in the He-shielding gas interface [51], which results in a significant

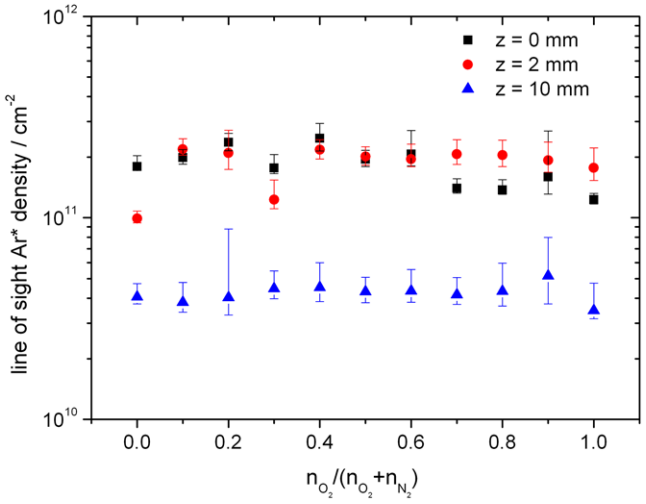

Figure 6. Line-of-sight Ar* density in dependence on the oxygen/nitrogen ratio in the shielding gas for three different axial positions.

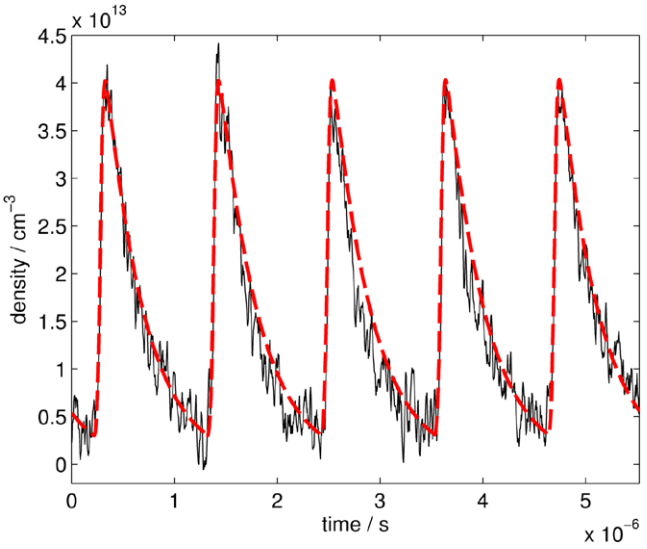

Figure 7. Ar*-density obtained from LAAS measurements (black line) and from the electron impact plasma reaction kinetics model (red dashed line).

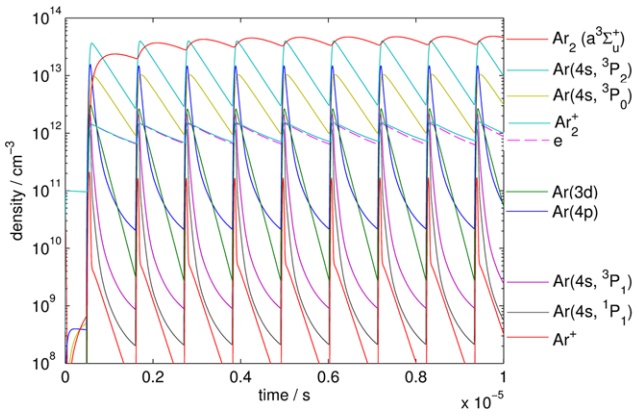

Figure 8. Denities of argon species considered in the electron impact model.

drop of metastable He concentration [52]. A similar mechanism may exist for Ar-operated jets, however this requires further investigation and cannot be stated based on the present statistical evaluation. Assuming an homogeneous absorber distribution within a filament of 100 μm, the peak Ar* density drops from 2×10^{13} cm^{-3} to 4×10^{12} cm^{-3} for an increase of the axial position from $z = 0$ to $z = 10$ mm, respectively.

Figure 7 shows a closeup of the Ar* density obtained from an LAAS measurement assuming 100 μm absorption length at a distance of 2 mm from the nozzle. As shown in figure 2 the Ar* absorption signal is subject to strong temporal fluctuations due to the turbulent flow and filamentary nature of the discharge. In order to receive a clean excitation pattern over several periods, the oscilloscope was triggered to a high absorption signal. The magnitude $A = 4614$ W cm^{-3} and pulse width $\tau = 3 \times 10^{-8}$ s of the power input (7) of the electron impact model was fitted to match the Ar* densities obtained experimentally. A good agreement of the decay of the Ar* was obtained assuming an air mole fraction of 5×10^{-4}.

In figure 8 all argon species included in the model are shown for several periods. The model reaches a steady state after a few periods. The argon excimer Ar_2^* is the most abundant argon species. It is entirely generated from the excited Ar states in three body reactions E19-E21. The measured state Ar(4s,^{3}P$_2$) is the dominant excited Ar state and also the major source of Ar_2^*. The Ar(4s,^{3}P$_0$) metastable state reaches approximately 25% of the Ar(4s,^{3}P$_2$) density. The densities of other states are comparably low. The sum of Ar(4p) states also reach similar densities, however they quickly radiate forming 4*s* states and hence can hardly contribute to the production of RONS. The dominant ion is Ar_2^+ with densities of $Ar_2^+ \approx n_e \approx 10^{12}$ cm^{-3}.

In figure 9 the electron density, electron temperature and input power obtained from the model are shown for different mole fractions of synthetic air. Note, that while the maximum power density in the model reaches more than 4500 Wcm^{-3} and is much higher than in previous kinetic studies, the average power density of 222 Wcm^{-3} is comparable to the values found in the literature for similar CAP devices: Van Gaens *et al* used a continuous power input of around 250 Wcm^{-3} in the plasma plume of argon CAP jets [21], Moravej *et al* used up to 150 Wcm^{-3} [53]. The electron density of 10^{12} cm^{-3} is in reasonable agreement with previous experimental studies: Taghizadeh *et al* measured electron densities of around 10^{12}–10^{13} cm^{-3} in the plume of an argon CAP jet by measuring its continuum radiation. Van Gessel *et al* measured higher electron densities of around 10^{13}–10^{14} cm^{-3} in the plume of an argon-operated CAP jet by Thomson scattering [54]. In that study also the electron temperature was measured by Thomson scattering and values between $T_e = 1$ eV to 1.5 eV were obtained. However, due to the duration of the laser pulse employed in the measurement, the authors state that mainly bulk electrons in the low electric field region behind the ionization front contribute to the Thomson scattering signal. Taghizadeh also determined the electron temperature in the plume of an argon CAP jet [55] and received similar values of around 1 eV combining spectroscopic measurements with a collisional radiative model.

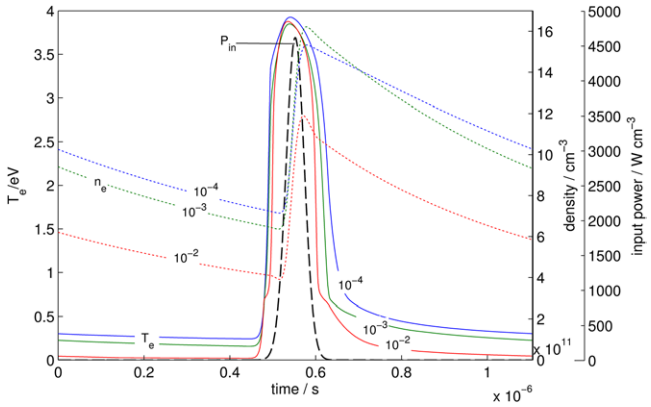

Figure 9. Electron temperature (left y-axis) and electron density (first y-axis on the right) obatined for the specified input power (second y-axis on the right) and three different mole fractions of synthetic air ($x_{\mathrm{air}} = 10^{-4}, 10^{-3}, 10^{-2}$).

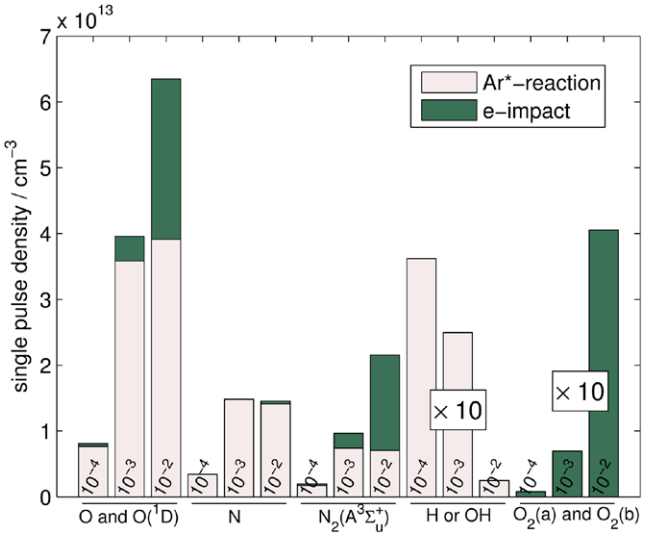

Figure 10. Density of various primary RONS generated by a single guided streamer at dry synthetic air mole fractions 10^{-4}, 10^{-3} and 10^{-2}. Contributions from direct electron impact reactions and reactions involving excited argon species are distinguished.

Schäfer *et al* reported electron densities in the range of some 10^{14} cm^{-3} and temperatures of 2–3 eV in a RF argon plasma jet operated at 27 MHz [56]. A space resolved numerical model of a single filament of the plasma source yielded comparable values of $n_e = 7 \times 10^{13}$ cm^{-3} and $T_e = 1.9$ eV [56, 57]. Balcon *et al* investigated α to γ mode switching in a capacitive plane-to-plane micro discharge operated at 13.56 MHz using a 1D numerical model and obtained values of $n_e = 10^{12}$ cm^{-3} and $T_e = 2.5$–4 eV [58].

The recent numerical study for the argon-operated kinpen by van Gaens *et al* yielded an electron temperature of 3.2 eV and densities of 2×10^{11} cm^{-3} in the plasma plume. In our study we receive much higher temperatures of 3.9 eV. The difference arises from the short pulses we apply in our model: Running our model with a continuous power input of 220 Wcm^{-3} (same as for our pulsed study), we receive similar values of $T_e = 3.4$ eV and $n_e = 5 \times 10^{11}$ cm^{-3}. Comparing the effect of the different air concentrations in figure 9, it is observed that the maximum electron temperature during the short pulse is not significantly affected. With higher air concentration, the electron density decreases and the electron temperature drops faster after the pulse. This is associated to electron attachment to O_2 and rotational and vibrational energy losses. However, these studies were performed with the same power input. Whether the power input does actually reach similar values at positions where the air concentration is high, cannot be answered by a zero-dimensional model.

The main goal of the electron impact model is to determine how primary reactive species are generated from O_2, N_2 and H_2O. For this purpose the number of the most abundant primary RONS generated by a single pulse were evaluated for different mole fractions of air as shown in figure 10. Furthermore, the contributions from Ar*-reactions such as

$$\mathrm{X}^* + \mathrm{O}_2 \rightarrow 2 \cdot \mathrm{O} + \text{products}, \qquad \text{(R4/14)}$$

where X* denotes Ar* (R4), Ar_2^* (R14) and electron impact reactions, e.g.

$$\mathrm{e} + \mathrm{O}_2 \rightarrow \mathrm{e} + \mathrm{O} + \mathrm{O}(^1\mathrm{D}), \qquad \text{(E43)}$$

are distinguished. Note that here the states O and $O(^1D)$ as well as O_2(a) and O_2(b) are grouped. Additionally, fast radiative decay from N_2(B/C) to N_2(A) is assumed. In the dissociative electron attachment reactions of H_2O (E50 and E51) where H^- and OH or OH^- and H are formed a fast recombination of the anions to neutrals is assumed as found by van Gaens and Bogaerts [21]. It is observed, that for the given power input, most primary RONS are generated from reactions involving Ar* rather than from direct electron impact reactions. This does not apply for the low-energy (0.98 eV / 1.63 eV) O_2(a/b) states. It is assumed that due to their low energy these states do not dominantly contribute to the formation of RONS in the plasma plume of CAP jets. Therefore, merely using an Ar* source term to model the energy input in the plume of this CAP jet is a valid simplification to describe the resulting RONS chemistry. Figure 10 also shows that a significant amount of primary RONS is generated even when the mole fraction of air is 10^{-3} and lower, highlighting the importance of molecular impurities for the plasma chemistry in such CAP sources.

3.2. Reactive species output in the far field

The densities obtained by FTIR spectroscopy and from the neutral reactive species model are shown in figure 11 for shielding gas compositions ranging from pure N_2 to pure O_2. The magnitude of the Ar* source term (10) was varied until quantitative agreement of the computed and measured O_3 densities was obtained. Very good agreement was obtained for O_3, NO_2 and N_2O_5. For N_2O the dynamics was predicted correctly by the model, however the measured N_2O density is lower by a factor of 0.4. HNO_2 was predicted to be generated in measurable amounts by the model but was not detected. It was found that the sum of the computed HNO_2 and HNO_3 densities give the correct amount of HNO_3 as measured. The reaction mechanisms leading to the production of these RONS and possible reasons for the observed deviation of model and measurements are discussed in the following. Also CO_2 and CO

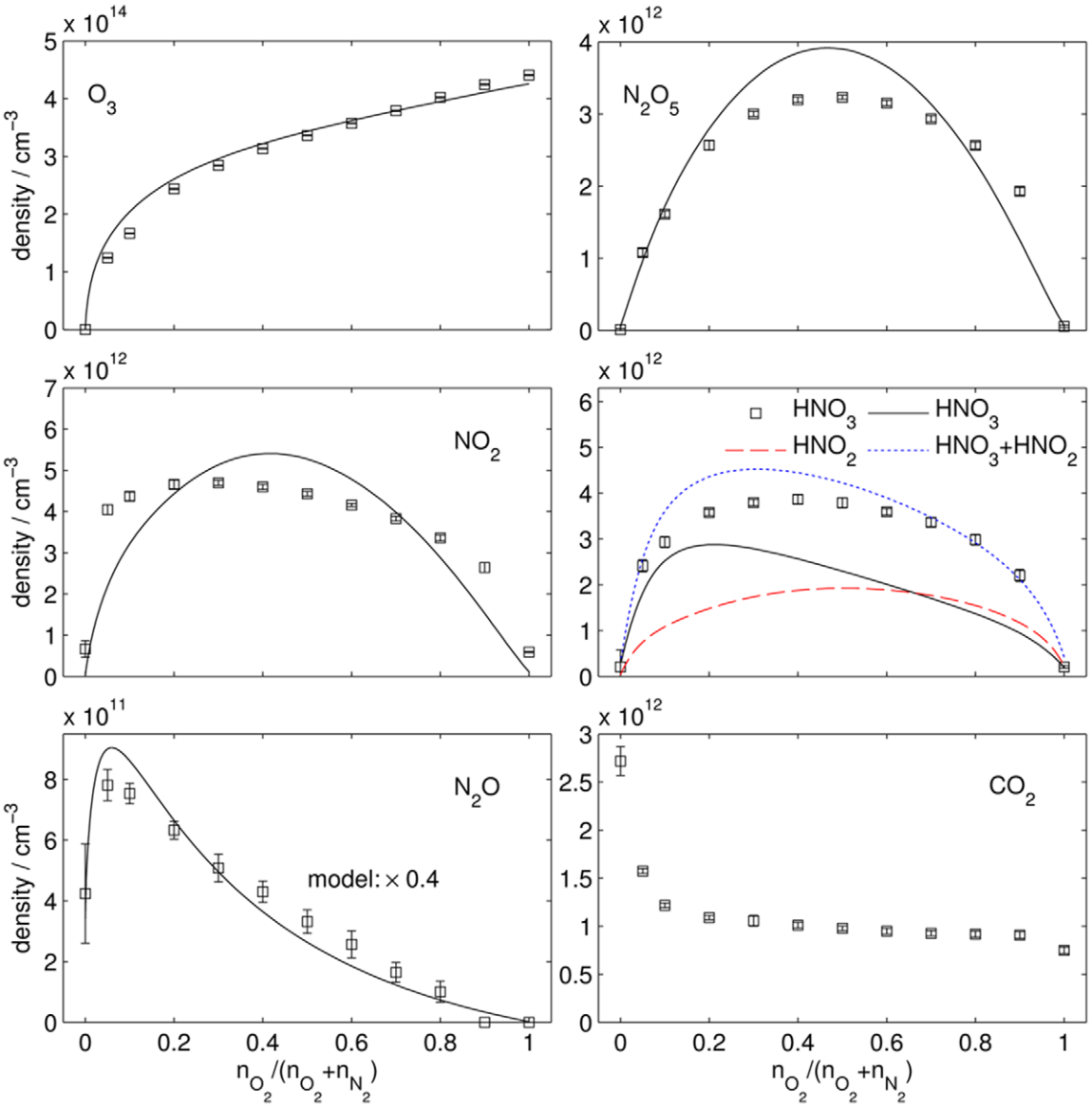

Figure 11. Reactive species densities obtained from FTIR spectroscopy and numerical model versus shielding gas composition. All densities were multiplied by 10/6 in order to be comparable to measurements obtained at standard pressure.

were detected. According to manufacturer specifications the argon feed gas contains up to 0.2 ppm hydrocarbons which is probably the main source for the measured CO_2. The increase of CO_2 at 0% O_2 content in the shielding gas is significant and was confirmed in several measurements. The cause for this increase is unclear. One assumption is that N_2^* exists longer if O_2 (being a major quencher of N_2^* through reactions R23 and R26) is absent and hence N_2^* may provide the energy necessary for cracking the hydrocarbons. Also CO impurities in the N_2 shield gas were detected at a density of 8×10^{12} cm^{-3}. However, CO is not expected to influence the further RONS chemistry as the density at the position of the guided streamer is negligible and it is unlikely to significantly influence the downstream reaction chemistry due to its large bond energy of 11.2 eV. Accordingly no significant consumption of CO was observed.

In figure 12(a) the absorbance between $\nu = 1220$ cm^{-1} and 1320 cm^{-1} is shown as measured using synthetic air as shielding gas ($O_2/N_2 = 0.2$). As the absorption profile of H_2O_2 is superposed by N_2O_5 and HNO_3, H_2O_2 could not be clearly identified in the FTIR measurements. However, as the model suggests that it should be present, its cross section was included in the fitting routine. The respective densities obtained are shown in figure 12(b). While the quantitative agreement of kinetic model and FTIR results is acceptable, it is unclear if the differences upon shielding gas variation arise from shortcomings of the kinetic model or correlations of the H_2O_2 absorption profile with the N_2O_5 and HNO_3 profiles in the fitting process. Note that model and FTIR data agree well for pure O_2 and pure N_2, when no HNO_3 and N_2O_5 are generated.

The magnitude of the local Ar^* source term obtained in this model is seven times lower than the source term obtained in the electron impact reaction kinetics model, while the total (volume integrated) production rate is 14 times higher as in the electron impact model due to the different radii of volume

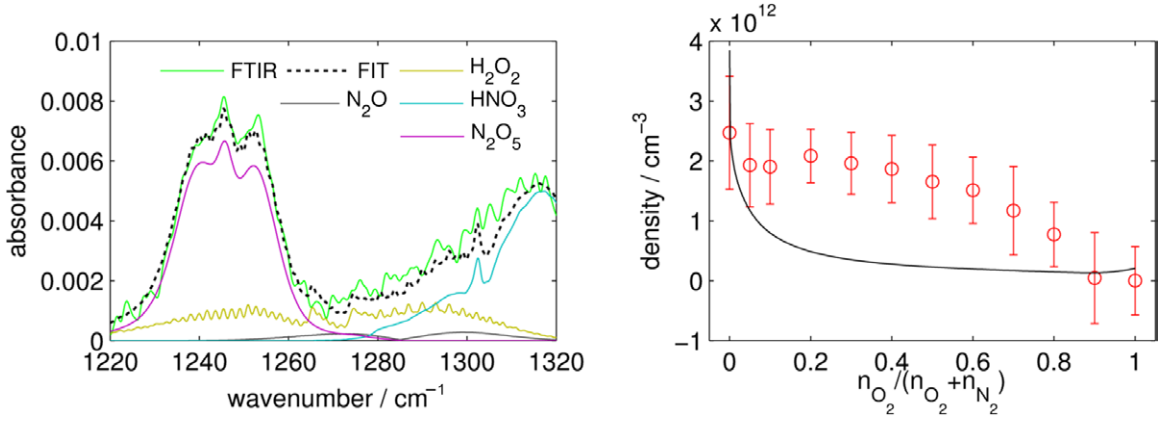

Figure 12. Measured and fitted absorbance of H_2O_2 (a) and respective densities obtained from the fit and the numerical model (b).

elements considered. A perfect agreement of both the production rates can be achieved by choosing the estimated diameters of the guided streamer (for the electron impact model) and the diffusive RONS channel (for the neutral reaction chemistry model) accordingly. However, this was not done as the total RONS output is affected by several parameters, e.g. the detailed shielding gas density at the position of the streamer (see figure 10), the assumed length of the discharge and the flow velocity.

3.3. Reaction pathways

In figure 13 the densities of reactive species are shown as computed for the plasma plume (a), glass chamber (b) and MPC (c). From the simulation it is obvious that the species composition measured in the far field of plasma sources by FTIR spectroscopy is very different from the species that can be expected in the plasma plume.

3.3.1. Reaction mechanisms: O and O_3. The generation of O_3 is determined by the three-body reaction

$$O + O_2 + M \rightarrow O_3 + M, \qquad \text{(R43)}$$

where M is an arbitrary reaction partner. The relevant generation and destruction mechanisms for O are illustrated in figure 14. In this and the following figures, the densities of the respective species generated through the indicated reactions is shown as positive values, the densities consumed when the species is a reactant is given as negative values. Only the reactions significantly contributing to the generation and destruction processes are shown. In the plasma plume, O is generated from the dissociation of O_2 from excited species in the reactions

$$X^* + O_2 \rightarrow 2 \cdot O + \text{products}, \qquad \text{(R4/14/23)}$$

where X^* denotes Ar^* (R4), Ar_2^* (R44) and N_2^* (R46). Besides the formation of O_3, O can also be lost via reactions with OH and HO_2 (reactions R44 and R46). In the glass chamber additional O is generated (to a lesser extent) from reactions of N with NO (R42) and O_2.

3.3.2. Reaction mechanisms: NO. The relevant generation and destruction mechanisms for NO are illustrated in figure 15. The main reaction leading to the generation of NO in the plasma plume and glass chamber is

$$N + OH \rightarrow NO + H \qquad \text{(R64)}$$

which is one of the reactions of the extended Zeldovich mechanism e.g. relevant for NO generation in combustion processes [59]. To a lesser extent, NO is also generated via the reaction of N_2^* and O (R86) and in the three body reaction of O with N (R38). Note that in the work of van Gaens and Bogaerts [21] R86 is the main reaction contributing to NO generation. The pathways differ as in [21] N_2^* reaches densities of $2 \times 10^{14}\text{cm}^{-3}$ which is 5 times higher than in our model, while in our model the Ar^* density is more than ten times higher than in [21]. The high Ar^* density yields significant amounts of N and consequently promotes reaction R64. N also leads to loss of NO by reacting to N_2 and O (R42). Further NO destruction mechanisms lead to the production of NO_2 and are discussed in the following.

3.3.3. Reaction mechanisms: NO_2. As illustrated in figure 16, many reactions contribute to the generation and destruction of NO_2 in the plasma plume and glass chamber. However, most NO_2 is generated through the oxidation of NO in reactions of the form

$$NO + Y \rightarrow NO_2 + \text{products}, \qquad \text{(R49/R74/R72)}$$

where Y denotes O (R49, involving a third body), O_3 (R72) or HO_2 (R74). Further important mechanisms for the NO_2 generation and destruction involve HNO_x and N_2O_5 and are discussed below.

3.3.4. Reaction mechanisms: N_2O. For N_2O only two processes were found to be important on the relevant timescale as illustrated in figure 17: In the plasma plume the reaction

$$N_2^* + O_2 \rightarrow N_2O + O \qquad \text{(R26)}$$

dominates, while in the glass chamber further N_2O is generated from the reaction of NO_2 and N (R35). The model predicts more than twice the amount of N_2O than what is measured via FTIR spectroscopy. A possible explanation is that R26 is exclusively responsible for the generation of N_2O, yielding the right quantity and dynamics under shielding gas variation. The reason for an overestimation of R35 could be, that mixing

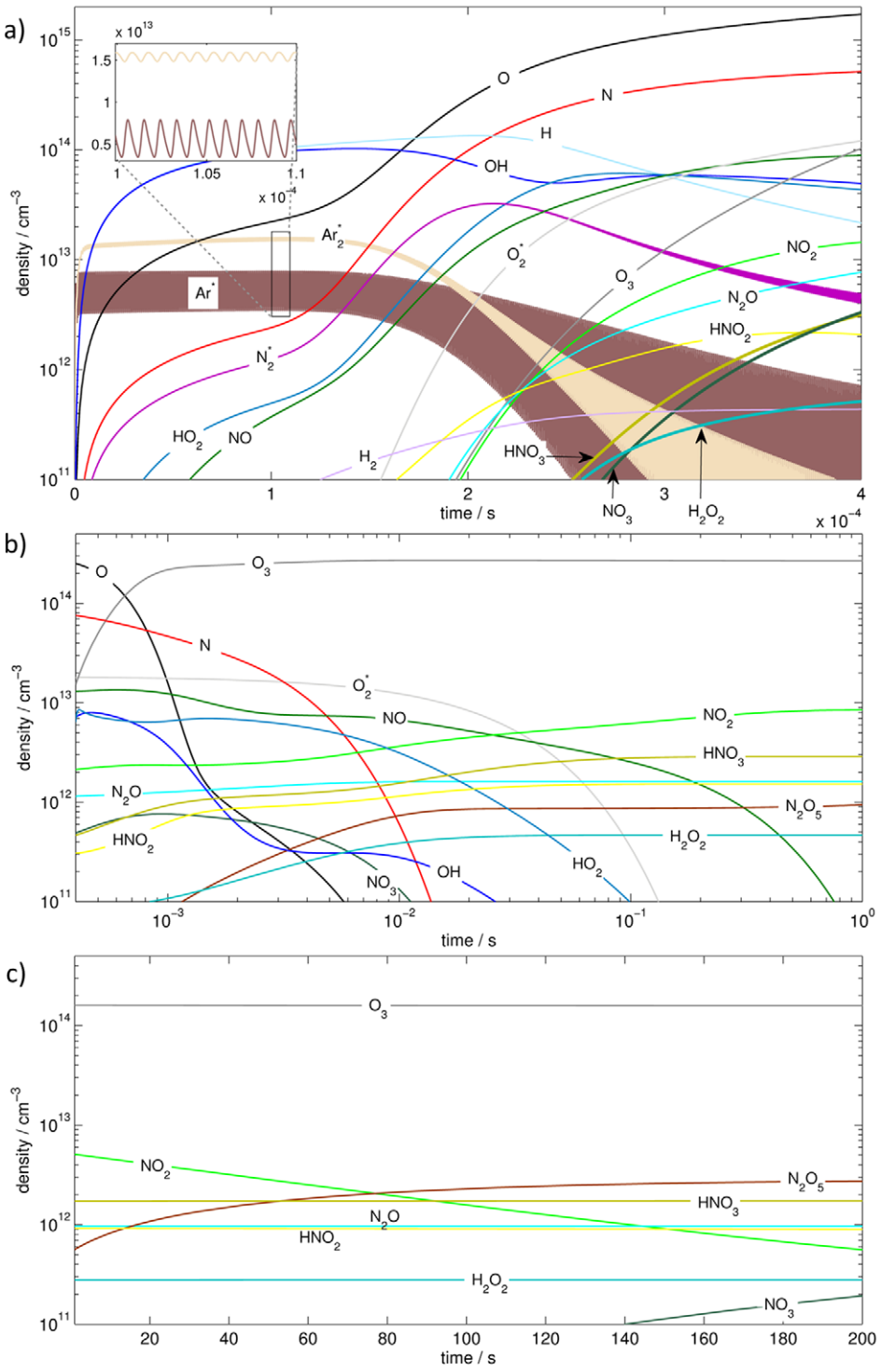

Figure 13. Computed temporal development of reactive species in the plasma plume (a), glass chamber (b) and MPC (c) using synthetic air as shielding gas.

in the glass chamber occurs faster than described by the diffusion source term (9), promoting the reaction

$$\mathrm{N} + \mathrm{O_2} \rightarrow \mathrm{NO} + \mathrm{O} \qquad \text{(R34)}$$

which effectively removes N, inhibiting reaction R35. Omitting R35 would also give better agreement of NO_2 model and experimental results, yielding higher NO_2 densities for low oxygen content in the shielding gas (see figure 4).

3.3.5. Reaction mechanisms: HNO_2 *and* HNO_3. In figure 18 the relevant reaction mechanisms for both HNO_2 and HNO_3 are shown. HNO_2 and HNO_3 are generated via the processes

$$\mathrm{NO_x} + \mathrm{OH} + \mathrm{M} \rightarrow \mathrm{HNO_{x+1}} + \mathrm{M}. \qquad \text{(R73/67)}$$

HNO_2 can be converted to HNO_3 in a two-step process, where

$$\mathrm{HNO_2} + \mathrm{O} \rightarrow \mathrm{OH} + \mathrm{NO_2} \qquad \text{(R83)}$$

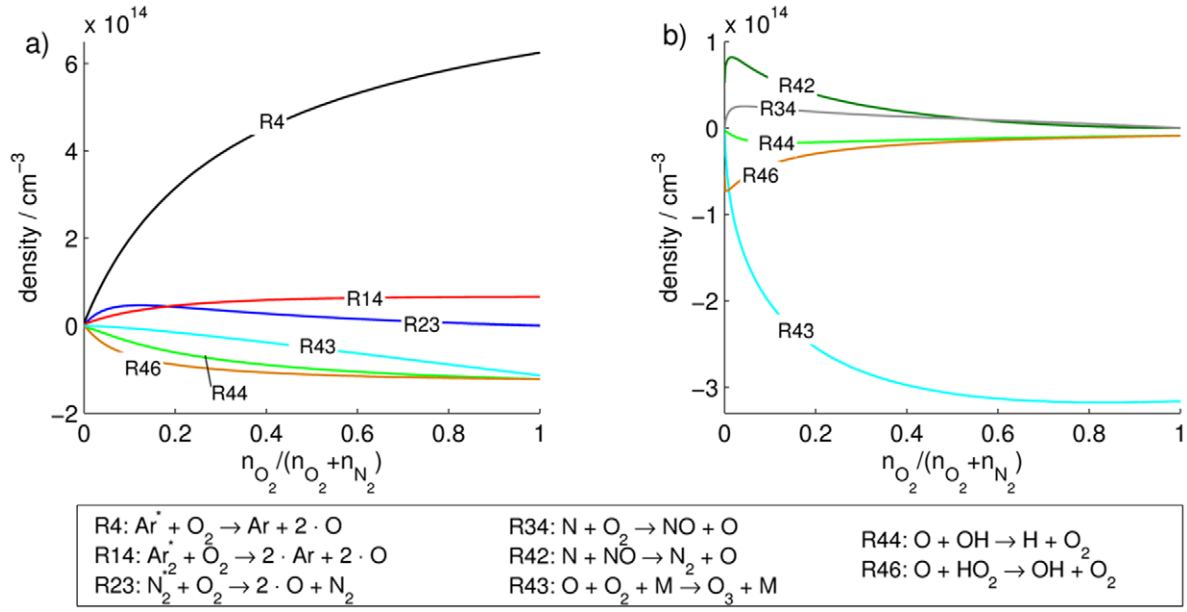

Figure 14. Main reactions contributing to generation and destruction of O in the plasma plume (a) and glass chamber (b).

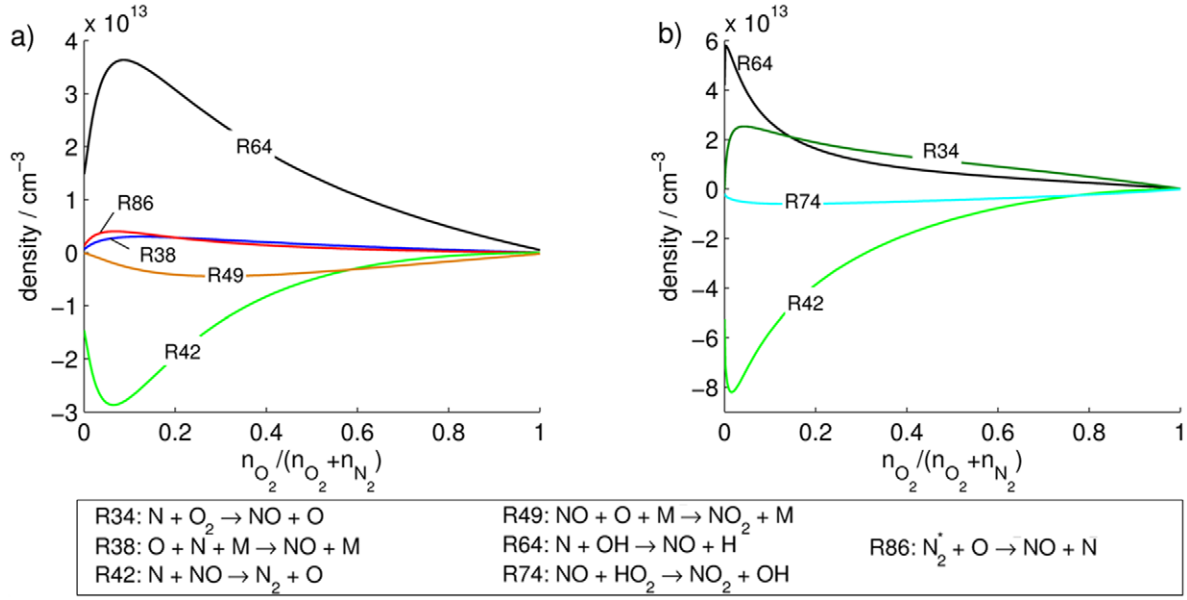

Figure 15. Main reactions contributing to generation and destruction of NO in the plasma plume (a) and glass chamber (b).

yields the reactants for R67. Since the sum of the densities of HNO_2 and HNO_3 computed in the kinetic model add up to the correct value of HNO_3 measured via FTIR spectroscopy, we assumed that the conversion process R83 is underestimated in the model. The reason for this was assumed to be that O_2^* is underestimated in the model, which can be generated directly in electron impact reactions. It is well-known, that O_2^* can recycle a fraction of O_3 to O (R55), which could then initiate the conversion process of HNO_2 R83 and R67. For this reason a simulation was run with an additional O_2^* source term producing 10^{12} cm^{-3} O_2^* every period in the plasma plume (compare results of electron-impact study shown in figure 10), but the far-field species obtained were hardly affected. Another possibility is, that NO is converted to NO_2 faster than predicted by the model and hence HNO_3 is generated rather than HNO_2.

3.3.6. Reaction mechanisms: N_2O_5. In the MPC the only relevant reaction mechanism on this timescale is the generation of N_2O_5 from NO_2 in a two-step process as shown in figure 19: First NO_3 is formed from NO_2 and O_3 which is available in abundance in the reaction

$$NO_2 + O_3 \rightarrow NO_3 + O_2, \qquad \text{(R81)}$$

which then reacts to N_2O_5:

$$NO_2 + NO_3 + M \leftrightarrow N_2O_5 + M \qquad \text{(R78/79)}$$

For longer timescales reactions R78 and R79 result in an equilibrium which can yield significant amounts of NO_3, a process relevant in dielectric barrier discharges that are not flow-driven [19].

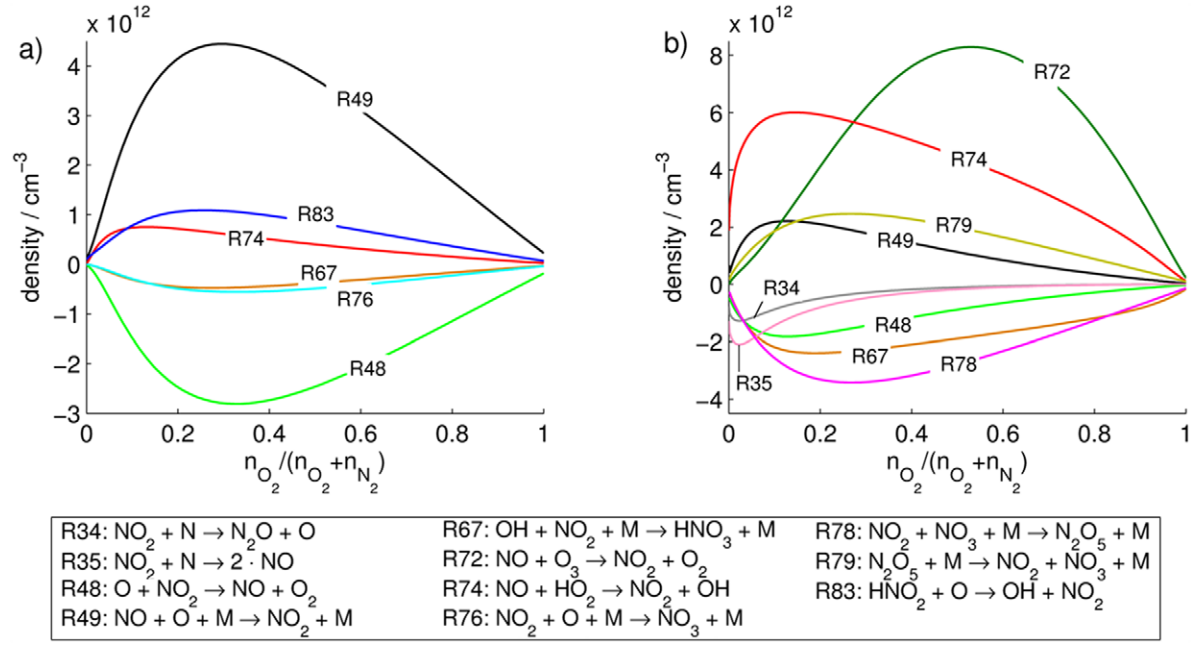

Figure 16. Main reactions contributing to generation and destruction of NO_2 in the plasma plume (a) and glass chamber (b).

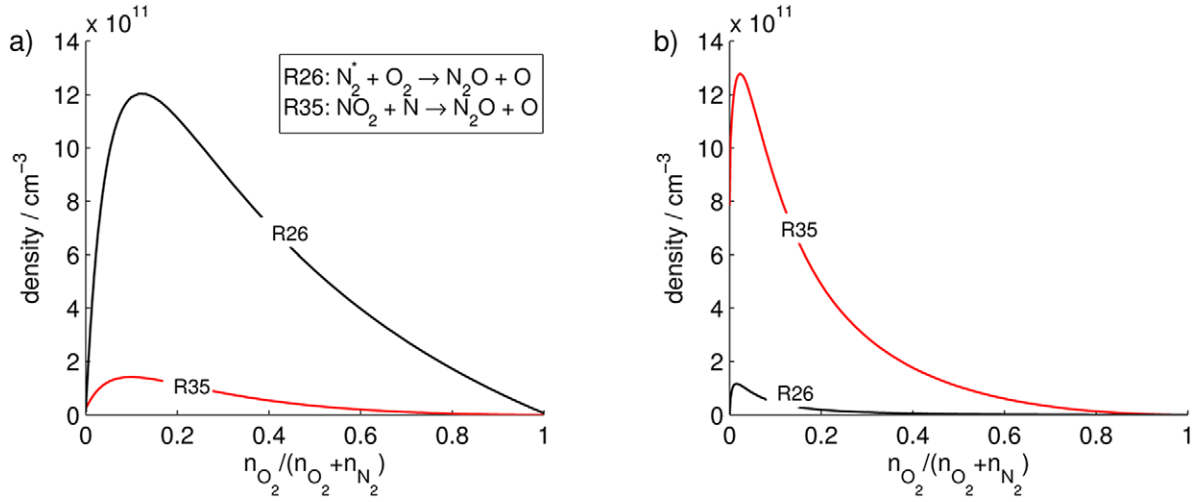

Figure 17. Main reactions contributing to generation and destruction of N_2O in the plasma plume (a) and glass chamber (b).

4. Conclusion

In this work the reaction kinetics leading to the generation or RONS in an argon-operated CAP jet operated with shielding gas device were investigated. Experimental data of RONS densities obtained by FTIR spectroscopy in the far-field and Ar^* densities measured by LAAS in the plasma plume is combined with zero-dimensional modeling of the reaction kinetics using two separate models. The fast and localized generation of primary reactive species in the guided streamer head is evaluated using a first electron impact reaction kinetics model, while the further plasma chemical processes in the visible plasma plume and the downstream region (e.g. inside the measurement apparatus) is considered in a second neutral reaction kinetics model. A parametric study is performed varying the shielding gas composition from pure N_2 to pure O_2.

The Ar^* densities obtained by the first electron impact model were fitted to the densities obtained by LAAS. It was found, that Ar^* is the main source of primary RONS in the plasma plume. The model yields a maximum electron temperature of 3.9 eV during the pulse and an electron density in the order of 10^{12} cm^{-3}.

The O_3 density computed by the second neutral reaction chemistry model was fitted to the density obtained from FTIR measurements using the magnitude of an Ar^* source term as

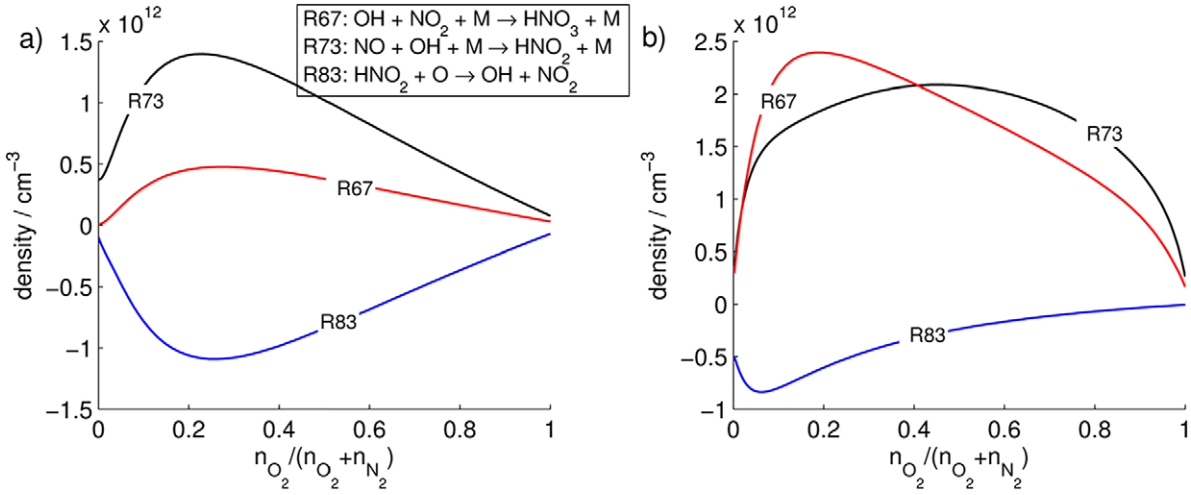

Figure 18. Main reactions contributing to generation and destruction of HNO_2 and HNO_3 in the plasma plume (a) and glass chamber (b).

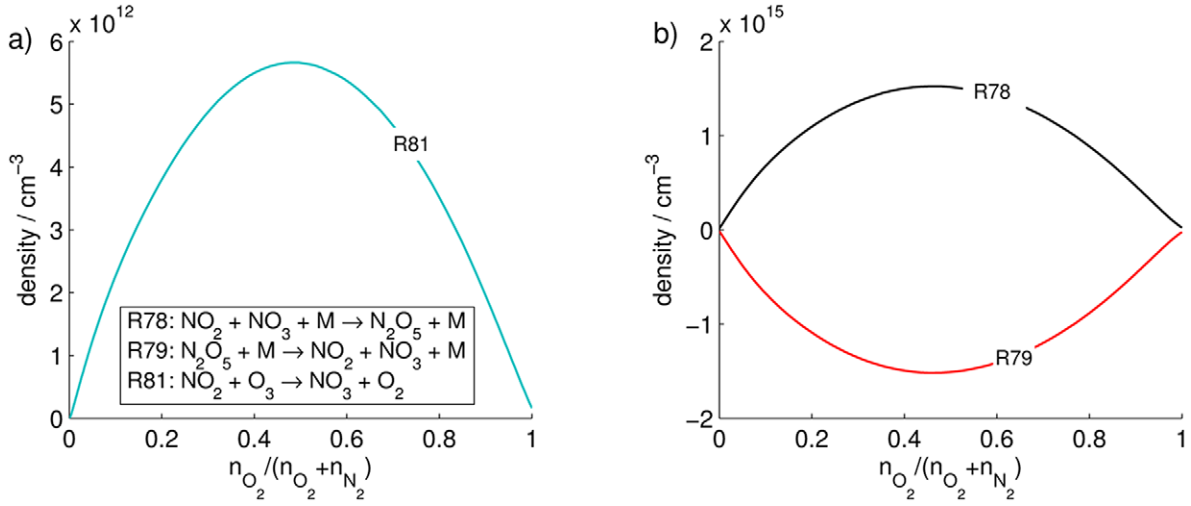

Figure 19. Main reactions contributing to generation and destruction of NO_3 (a) and N_2O_5 (b) in the MPC.

free parameter. The influence of this and further free parameters is discussed in the appendix B. The densities of other RONS predicted by the model (NO_2, N_2O_5, N_2O, HNO_3 and H_2O_2) are in good agreement with the FTIR measurements.

For the here-investigated CAP jet operating with pure Ar as feed gas, it was found that it is sufficient to use Ar^* as sole input species for the neutral reaction kinetics model. However, the approach can be extended to suit for a broader class of devices, also when using molecular admixtures, by considering the complete set of primary reactive species (also including ions if necessary) generated in quantities as predicted by the electron impact reaction kinetics model. The approach is especially suitable for performing large parametric studies and can hence be used to optimize the reactive species generation of CAP jets for the respective field of application, such as plasma medicine or surface modification.

Acknowledgments

The authors would like to thank Y Sakiyama and D Graves for fruitful discussions. The work on the reaction kinetics models was started during a stay of A Schmidt-Bleker at Prof Graves lab at the University of California at Berkeley. This work was supported by the German Ministry of Education and Research (BMBF, Grant No. 03Z2DN12).

Appendix A. Reactions considered in the model

Table A1. List of reactions used in the electron impact model.

ID	Reaction	Rate coefficient	Reference
E1	$e + Ar \rightarrow e + Ar$	$\sigma(\epsilon)$	[61]
E2	$e + Ar \rightarrow 2 \cdot e + Ar^+$	$\sigma(\epsilon)$	[61]
E3	$e + Ar \rightarrow e + Ar(4s, {}^3P_2)$	$\sigma(\epsilon)$	[61]
E4	$e + Ar \rightarrow e + Ar(4s, {}^3P_1)$	$\sigma(\epsilon)$	[61]
E5	$e + Ar \rightarrow e + Ar(4s, {}^3P_0)$	$\sigma(\epsilon)$	[61]
E6	$e + Ar \rightarrow e + Ar(4s, {}^1P_1)$	$\sigma(\epsilon)$	[61]
E7	$e + Ar \rightarrow e + Ar(4p)$	$\sigma(\epsilon)$	[62]
E8	$e + Ar \rightarrow e + Ar(3d)$	$\sigma(\epsilon)$	[62]
E9	$Ar(4s, {}^3P_1) \rightarrow Ar$	$1.19\ 10^8$	[63]
E10	$Ar(4s, {}^1P_1) \rightarrow Ar$	$5.1\ 10^8$	[63]
E11	$Ar(4p) \rightarrow Ar(4s, {}^3P_2)$	$5\ 10^6$	[63][a]
E12	$Ar(4p) \rightarrow Ar(4s, {}^3P_1)$	$5\ 10^6$	[63][a]
E13	$Ar(4p) \rightarrow Ar(4s, {}^3P_0)$	$5\ 10^6$	[63][a]
E14	$Ar(4p) \rightarrow Ar(4s, {}^1P_1)$	$5\ 10^6$	[63][a]
E15	$Ar(3d) \rightarrow Ar(4p)$	$5\ 10^6$	[63][a]
E16	$Ar_2^+ + e \rightarrow Ar + Ar(4p)$	$8\ 10^{-7}(300/T_e)^{2/3}$	[64]
E17	$Ar^+ + Ar + M \rightarrow Ar_2^+ + M$	$2.5\ 10^{-31}$	[21]
E18	$2 \cdot Ar(4s, {}^3P_2) \rightarrow Ar^+ + Ar + e$	$5\ 10^{-10}$	[53]
E19	$Ar(4p) + Ar + M \rightarrow Ar_2(a^3\Sigma_u^+) + M$	$1\ 10^{-31}$	[21]
E20	$Ar(3d) + Ar + M \rightarrow Ar_2(a^3\Sigma_u^+) + M$	$1\ 10^{-31}$	[21]
E21	$Ar(4s) + Ar + M \rightarrow Ar_2(a^3\Sigma_u^+) + M$	$2.8\ 10^{-33}$	[65][b]
E22	$Ar_2(a^3\Sigma_u^+) + Ar \rightarrow 3 \cdot Ar$	10^{-14}	[66][c]
E23	$Ar_2(a^3\Sigma_u^+) \rightarrow 2 \cdot Ar$	$3.5\ 10^5$	[65, 67]
E24	$e + N_2 \rightarrow e + N_2$	$\sigma(\epsilon)$	[68]
E25	$e + N_2 \rightarrow e + N_2(vib/rot)$	$\sigma(\epsilon)$	[68][d]
E26	$e + N_2 \rightarrow e + N_2(B^3\Pi_g)$	$\sigma(\epsilon)$	[68]
E27	$e + N_2 \rightarrow e + N_2(W^3\Delta_u)$	$\sigma(\epsilon)$	[68]
E28	$e + N_2 \rightarrow e + N_2(A^3\Sigma_u^+)$	$\sigma(\epsilon)$	[68]
E29	$e + N_2 \rightarrow e + N_2(B'^3\Sigma_u^-)$	$\sigma(\epsilon)$	[68]
E30	$e + N_2 \rightarrow e + N_2(a'^1\Sigma_u^-)$	$\sigma(\epsilon)$	[68]
E31	$e + N_2 \rightarrow e + N_2(a^1\Pi_g)$	$\sigma(\epsilon)$	[68]
E32	$e + N_2 \rightarrow e + N_2(w^1\Delta_u)$	$\sigma(\epsilon)$	[68]
E33	$e + N_2 \rightarrow e + N_2(C^3\Pi_u)$	$\sigma(\epsilon)$	[68]
E34	$e + N_2 \rightarrow e + 2 \cdot N$	$\sigma(\epsilon)$	[68]
E35	$e + N_2 \rightarrow 2 \cdot e + N_2^+$	$\sigma(\epsilon)$	[68]
E36	$e + O_2 \rightarrow O + O^-$	$\sigma(\epsilon)$	[69]
E37	$e + O_2 \rightarrow e + O_2$	$\sigma(\epsilon)$	[69]
E38	$e + O_2 \rightarrow e + O_2(vib/rot)$	$\sigma(\epsilon)$	[69]
E39	$e + O_2 \rightarrow e + O_2(a^1\Delta_g)$	$\sigma(\epsilon)$	[69]
E40	$e + O_2 \rightarrow e + O_2(b^1\Sigma_g^+)$	$\sigma(\epsilon)$	[69]
E41	$e + O_2 \rightarrow e + O(c^1, C^3, A^3)$	$\sigma(\epsilon)$	[69]
E42	$e + O_2 \rightarrow e + 2 \cdot O$	$\sigma(\epsilon)$	[69]
E43	$e + O_2 \rightarrow e + O + O(^1D)$	$\sigma(\epsilon)$	[69]
E44	$e + O_2 \rightarrow 2 \cdot e + O_2^+$	$\sigma(\epsilon)$	[69]
E45	$e + O_2 \rightarrow e + O + O^+$	$\sigma(\epsilon)$	[69]
E46	$e + H_2O \rightarrow e + H + OH$	$\sigma(\epsilon)$	[70]
E47	$e + H_2O \rightarrow e + O(^1D) + H_2$	$\sigma(\epsilon)$	[70]
E48	$e + H_2O \rightarrow e + H_2O^+$	$\sigma(\epsilon)$	[70]

(Continued)

Table A1. (Continued)

ID	Reaction	Rate coefficient	Reference
E49	$e + H_2O \rightarrow H_2 + O^-$	$\sigma(\epsilon)$	[70]
E50	$e + H_2O \rightarrow H^- + OH$	$\sigma(\epsilon)$	[70]
E51	$e + H_2O \rightarrow OH^- + H$	$\sigma(\epsilon)$	[70]

Note: The rate coefficients are given in units of s^{-1}, $cm^3\,s^{-1}$ or $cm^6\,s^{-1}$ for first, second or third order reactions. Rate coefficients for electron impact reactions were computed using BOLSIG + [60] with the cross section from the given reference.

[a] Estimated based on typical lifetimes of 4s and 3d states [63].

[b] Rate applied for all Ar(4s)-levels.

[c] Reaction yields $Ar_2^*(^1\Sigma_u^+)$, which dissociates quickly (lifetime 4.2ns [65]).

[d] All levels found in [68] were taken into account, but grouped into one level.

Table A2. List of reactions used in the electron impact model.

ID	Reaction	Rate coefficient	Reference
R1	$Ar^* + Ar + M \rightarrow Ar_2^* + M$	$2.8\ 10^{-33}$	[65]
R2	$Ar_2^* + Ar \rightarrow 3 \cdot Ar$	10^{-14}	[66][a]
R3	$Ar_2^* \rightarrow 2 \cdot Ar$	$3.5\ 10^{5}$	[65, 67]
R4	$Ar^* + O_2 \rightarrow Ar + 2 \cdot O$	$2.1\ 10^{-10}$	[71]
R5	$Ar^* + N_2 \rightarrow Ar + N_2^*$	$1.8\ 10^{-11}$	[71][b]
R6	$Ar^* + N_2 \rightarrow Ar + 2 \cdot N$	$1.8\ 10^{-11}$	[71][b]
R7	$Ar^* + H_2O \rightarrow Ar + OH + H$	$7.8\ 10^{-10}$	[72, 73]
R8	$Ar^* + O_3 \rightarrow Ar + O_2 + O^*$	$2.1\ 10^{-10}$	[21]
R9	$Ar^* + N_2^* \rightarrow Ar + 2 \cdot N$	$3.6\ 10^{-11}$	[21]
R10	$Ar^* + NO \rightarrow Ar + N + O$	$2.39\ 10^{-10}$	[21]
R11	$Ar^* + NO_2 \rightarrow Ar + NO + O$	$6.49\ 10^{-10}$	[21]
R12	$Ar^* + N_2O \rightarrow Ar + NO + N$	$4.4\ 10^{-10}$	[21]
R13	$Ar^* + N_2O \rightarrow Ar + N_2^* + O$	$4.4\ 10^{-10}$	[21]
R14	$Ar_2^* + O_2 \rightarrow 2 \cdot Ar + 2 \cdot O$	$4.6\ 10^{-11}$	[64]
R15	$Ar_2^* + N_2 \rightarrow 2 \cdot Ar + N_2^*$	$6\ 10^{-12}$	[66][c]
R16	$Ar_2^* + N_2 \rightarrow 2 \cdot Ar + 2 \cdot N$	$6\ 10^{-12}$	[66][c]
R17	$Ar_2^* + H_2O \rightarrow 2 \cdot Ar + OH + H$	$7.8\ 10^{-10}$	[72, 73][d]
R18	$Ar_2^* + O_3 \rightarrow 2 \cdot Ar + O_2 + O$	$2.1\ 10^{-12}$	[21]
R19	$Ar_2^* + NO \rightarrow 2 \cdot Ar + N + O$	$3.1\ 10^{-10}$	[21]
R20	$Ar_2^* + NO_2 \rightarrow 2 \cdot Ar + NO + O$	$8.44\ 10^{-10}$	[21]
R21	$Ar_2^* + N_2O \rightarrow 2 \cdot Ar + N_2 + O$	$5.5\ 10^{-10}$	[21]
R22	$2 \cdot N_2^* \rightarrow N_2^* + N_2$	$3.9\ 10^{-10}$	[74, 75][e]
R23	$N_2^* + O_2 \rightarrow 2 \cdot O + N_2$	$1.5\ 10^{-12}$	[76]
R24	$O_2^* + O_3 \rightarrow O + 2 \cdot O_2$	$5.2\exp(-2840/T_g)10^{-11}$	[77][f]
R25	$N_2^* + N \rightarrow N_2 + N$	$4\ 10^{-11}$	[78]
R26	$N_2^* + O_2 \rightarrow N_2O + O$	$7.8\ 10^{-14}$	[21]
R27	$N_2^* + N_2O \rightarrow 2 \cdot N_2 + O$	$9.3\exp(-120/T_g)10^{-12}$	[79][f]
R28	$N_2^* + N_2O \rightarrow NO + N + N_2$	10^{-11}	[21]
R29	$N_2^* + O \rightarrow O^* + N_2$	10^{-12}	[19]
R30	$N_2^* + Ar \rightarrow N_2 + Ar$	$4\ 10^{-17}$	[21]
R31	$N_2^* + N_2 \rightarrow 2 \cdot N_2$	$3.7\ 10^{-16}$	[21]
R32	$N_2^* + O_2 \rightarrow N_2 + O_2^*$	$1.29\ 10^{-12}$	[21]
R33	$O_2^* + N_2^* \rightarrow 2 \cdot O + N_2$	$2\ 10^{-11}$	[21]
R34	$N + O_2 \rightarrow NO + O$	$1.5\exp(-3600/T_g)10^{-11}$	[77][f]
R35	$NO_2 + N \rightarrow N_2O + O$	$1.4\ 10^{-12}$	[80][f]
R36	$NO_2 + N \rightarrow 2 \cdot NO$	$2.3\ 10^{-12}$	[20]
R37	$O + N + N_2 \rightarrow N_2 + NO$	$1.76\ T_g^{-0.5}10^{-31}$	[20]
R38	$O + N + M \rightarrow NO + M$	$5.46\exp(156/T_g)10^{-33}$	[81][f]
R39	$3 \cdot N \rightarrow N + N_2$	$3.31\ T_g^{-1.5}10^{-27}$	[20]

(Continued)

Table A2. (Continued)

ID	Reaction	Rate coefficient	Reference
R40	$2 \cdot N + Ar \rightarrow N_2 + Ar$	$1.25\ 10^{-32}$	[82][f]
R41	$HNO + O \rightarrow OH + NO$	$5.99\ 10^{-11}$	[83][f]
R42	$N + NO \rightarrow N_2 + O$	$2.1 \exp(96/T_g)10^{-11}$	[77][f]
R43	$O + O_2 + M \rightarrow O_3 + M$	$3.4(T_g/298)10^{-34}$	[76, 84]
R44	$O + OH \rightarrow H + O_2$	$2.4 \exp(108.2/T_g)10^{-11}$	[85][f]
R45	$O + O_3 \rightarrow 2 \cdot O_2$	$8.00 \exp(-2060/T_g)10^{-12}$	[85][f]
R46	$O + HO_2 \rightarrow OH + O_2$	$2.7 \exp(228.5/T_g)10^{-11}$	[85][f]
R47	$2 \cdot O + M \rightarrow O_2^* + M$	$6.93(T_g/300)^{-0.63}\ 10^{-35}$	[21]
R48	$O + NO_2 \rightarrow NO + O_2$	$5.5 \exp(192.4/T_g)10^{-12}$	[85][f]
R49	$NO + O + M \rightarrow NO_2 + M$	$9.02(T_g/298)^{-1.5}10^{-32}$	[77][f]
R50	$O^* + O_2 \rightarrow O + O_2$	$6.4 \exp(67/T_g)10^{-12}$	[19]
R51	$O^* + O \rightarrow 2 \cdot O$	$8\ 10^{-12}$	[19]
R52	$O^* + O_2^* \rightarrow O + O_2$	10^{-11}	[19]
R53	$O^* + O_2 \rightarrow O + O_2^*$	10^{-12}	[19]
R54	$O^* + O_3 \rightarrow 2 \cdot O + O_2$	$1.2\ 10^{-10}$	[19]
R55	$O^* + O_3 \rightarrow 2 \cdot O_2$	$1.2\ 10^{-10}$	[19]
R56	$O^* + N_2 \rightarrow O + N_2$	$1.8\ \exp(107/T_g)10^{-11}$	[19]
R57	$O^* + N_2 + M \rightarrow N_2O + M$	$3.5\ 10^{-37}(T_g/298)^{-0.6}$	[86][f]
R58	$O^* + N_2O \rightarrow N_2 + O_2$	$4.4\ 10^{-11}$	[19]
R59	$O^* + N_2O \rightarrow 2 \cdot NO$	$7.2\ 10^{-11}$	[19]
R60	$O^* + NO \rightarrow O + NO$	$4\ 10^{-11}$	[19]
R61	$O^* + NO_2 \rightarrow O_2 + NO$	$1.4\ 10^{-10}$	[19]
R62	$O^* + H_2O \rightarrow 2 \cdot OH$	$2.2\ 10^{-10}$	[19]
R63	$O^* + M \rightarrow O + M$	$5\ 10^{-12}$	[21]
R64	$N + OH \rightarrow NO + H$	$3.8 \exp(85/T_g)10^{-11}$	[87][f]
R65	$OH + HO_2 \rightarrow O_2 + H_2O$	$4.8 \exp(252.6/T_g)10^{-11}$	[85][f]
R66	$OH + O_3 \rightarrow HO_2 + O_2$	$1.7 \exp(-938.1/T_g)10^{-12}$	[85][f]
R67	$OH + NO_2 + M \rightarrow HNO_3 + M$	$2.2(T_g/298)^{-2.9}10^{-30}$	[87][f]
R68	$H + O_2 + M \rightarrow HO_2 + M$	$5.71(298/T_g)^{-1.6}10^{-32}$	[77][f]
R69	$2 \cdot HO_2 + M \rightarrow H_2O_2 + O_2 + M$	$1.7 \exp(999.5/T_g)10^{-33}$	[77][f]
R70	$2 \cdot OH + M \rightarrow H_2O_2 + M$	$6.2(T_g/298)^{-1}10^{-31}$	[77][f]
R71	$H_2O_2 + OH \rightarrow H_2O + HO_2$	$2.9 \exp(-156/T_g)10^{-12}$	[85][f]
R72	$NO + O_3 \rightarrow NO_2 + O_2$	$1.4 \exp(-1306/T_g)10^{-12}$	[85][f]
R73	$NO + OH + M \rightarrow HNO_2 + M$	$7(T_g/298)^{-2.6}10^{-31}$	[77][f]
R74	$NO + HO_2 \rightarrow NO_2 + OH$	$3.6 \exp(268/T_g)10^{-12}$	[85][f]
R75	$OH + HNO_2 \rightarrow NO_2 + H_2O$	$2.5 \exp(259/T_g)10^{-12}$	[85][f]
R76	$NO_2 + O + M \rightarrow NO_3 + M$	$9.0(T_g/298)^{-2}10^{-32}$	[77][f]
R77	$OH + HNO_3 \rightarrow NO_3 + H_2O$	$1.5 \exp(650./T_g)10^{-14}$	[86][f]
R78	$NO_2 + NO_3 + M \rightarrow N_2O_5 + M$	$2.81(T_g/298)^{-3.5}10^{-30}$	[86][f]
R79	$N_2O_5 + M \rightarrow NO_2 + NO_3 + M$	$3.7e^{-10039/T_g}10^{-5}$	[86][f]
R80	$2 \cdot H + M \rightarrow H_2 + M$	$6.04(T_g/298)^{-1}10^{-33}$	[88][f]
R81	$NO_2 + O_3 \rightarrow NO_3 + O_2$	$1.4 \exp(-2465/T_g)10^{-13}$	[85][f]
R82	$H + NO + M \rightarrow HNO + M$	$1.3(T_g/298)^{-1.32}e^{-370/T_g}10^{-31}$	[83][f]
R83	$HNO_2 + O \rightarrow OH + NO_2$	$2.01\ 10^{-11}$	[83][f]
R84	$HNO_2 + O_3 \rightarrow HNO_3 + O_2$	$5\ 10^{-19}$	[77][f]
R85	$HO_2 + NO + M \rightarrow HNO_3 + M$	$1.4\ 10^{-33}$	[89][f]
R86	$N_2^* + O \rightarrow NO + N$	$7\ 10^{-12}$	[21]
R87	$O_2 + O_2^* \rightarrow O_3 + O$	$3\ 10^{-21}$	[21]
R88	$2 \cdot O_2^* \rightarrow 2 \cdot O_2$	$9 \exp(-560/T_g)10^{-17}$	[21]
R89	$O_2^* + M \rightarrow O_2 + M$	$3 \exp(-200/T_g)10^{-30}$	[21]

(Continued)

Table A2. (Continued)

ID	Reaction	Rate coefficient	Reference
R90	$H + O_3 \rightarrow OH + O_2$	$1.4\exp(-470/T_g)10^{-10}$	[77][f]

Note: The rate coefficients are given in units of s^{-1}, $cm^3\,s^{-1}$ or $cm^6\,s^{-1}$ for first, second or third order reactions.

[a] Reaction yields $Ar_2^*(^1\Sigma_u^+)$, which dissociates quickly (lifetime 4.2ns [65]).

[b] Quenching rate of Ar^* by N_2 ($3.6 \cdot 10^{-11}\,cm^3\,s^{-1}$) is branched for creation of N_2^* and 2N.

[c] Quenching rate of Ar_2^* by N_2 ($1.2 \cdot 10^{-11}\,cm^3\,s^{-1}$) is branched to N_2^* and 2N.

[d] Estimation based on quenching rate for $Ar^* + H_2O$.

[e] These rates describe the energy pooling reactions for the formation of $N_2(B)$ and $N_2(C)$. Fast radiative relaxation to $N_2(A)$ from these levels is assumed.

[f] Rate obtained from NIST database [90]. The rate coefficient originates from the cited publication.

Appendix B. Sensitivity analysis of the gas phase reaction kinetics model

Even though the agreement of experimental data and the reaction kinetics model is good, this does not necessarily mean that all mechanisms presented here are correct. In the following the sensitivity of the model outcome is investigated by means of examples.

B.1. Different pathways can lead to similar far-field results

For the nitrogen oxides various reaction pathways can eventually lead to the same far-field species. This can for example be seen in figures 15 and 16, where the main reactions contributing to NO and NO_2 production and destruction are shown. In figure B1 the respective reactions leading to the generation of NO and NO_2 are summarized.

Even excluding the dominant reaction pathways for NO generation in the plasma plume via N (R38 and R64) and for NO_2 generation from NO (reactions R11 and R49) hardly affects the far-field species as shown in figure B2. In this case the generation proceeds mainly along the alternative pathways R86 and R83. Also, the oxidation of N to NO or of NO to NO_2 can occur via slower processes in the downstream region via alternative pathways: E.g. instead of oxidation of NO by O R49), in the plasma plume, the oxidation can also occur by reaction with O_3, which is available in high amounts in the downstream region (compare figure 15(b)).

B.2. The influence of free model parameters

Another issue is, that the model involves fitting parameters. The most obvious parameter is the magnitude of the Ar^* source term. However, this parameter mainly affects the magnitude of the RONS generated in the far-field, not the dynamic behavior upon shielding gas variation. The result for four parameters is given in the following: First, the influence of the Ar^* source term magnitude is discussed. Second, the influence of stronger and weaker shielding gas diffusion is studied. Third, the influence of feed gas humidity is discussed. Fourth, the influence of the branching ratio in the reactions

$$Ar^* + N_2 \rightarrow 2 \cdot N \text{ or } N_2^*, \qquad \text{(R5/6)}$$

as well as reactions

$$Ar_2^* + N_2 \rightarrow 2 \cdot Ar + 2 \cdot N \text{ or } N_2^*, \qquad \text{(R15/16)}$$

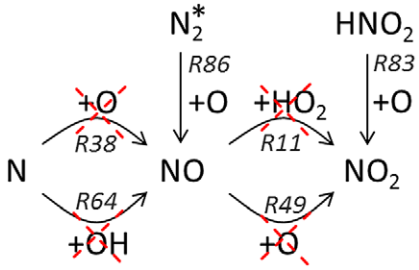

Figure B1. Main reaction pathways leading to the generation of NO and NO_2 in the plasma plume.

is studied (in the original work only the quenching ratio of Ar^*/Ar_2^* was given [66, 71]).

It is found, that general trends always agree with the experimental data, hence the validity of the presented model does not depend too strictly on the choice of open parameters: It is not possible to obtain any desired result by varying these parameters. The downside of this behavior is, that it is not possible to derive an exact value of the fitting parameters from the model results. E.g. the branching ratio of reactions R5/R6 does not influence the results enough to use the agreement of model and FTIR values as an indicator. Only significant changes and unexpected behavior compared to the basic study presented in section 3 are discussed below.

B.3. Influence of the Ar source term magnitude*

The densities obtained are shown in figure B3.

- Generally behaves as expected: The higher the Ar^* source term magnitude, the more RONS are generated.
- Exception: The NO_2 density does not change significantly. This occurs, as NO_2 is converted to N_2O_5, which is also present in higher quantities. Also, the destruction of NO with N (R42) damps the increased production of NO_2.

B.4. Influence of the shielding gas diffusion

The densities obtained are shown in figure B4.

- The more O_2 is present, the faster the conversion of O to O_3 (reaction R43).
- The formation of O from dissociation of O_2 by N_2^* is promoted, effecting the strong production of O_3 at low O_2 content in the shielding gas.

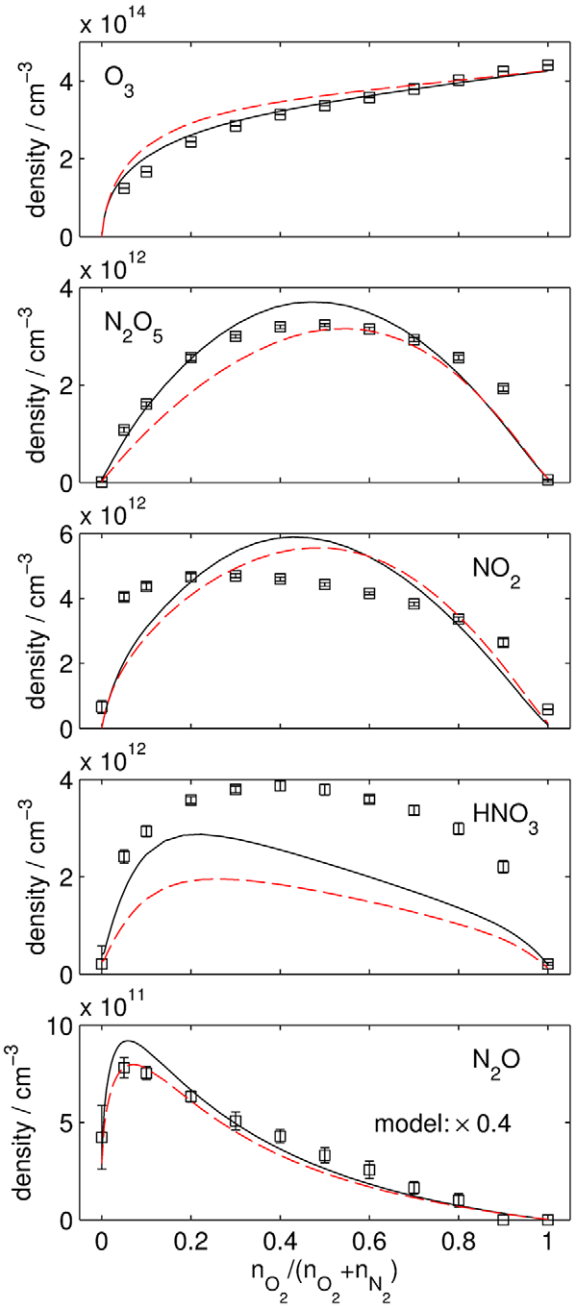

Figure B2. The black line reproduces the results shown in figure 11. The model results shown as red dashed line were obtained by setting reaction coefficients of reactions R11, R38, R49 and R64 to zero.

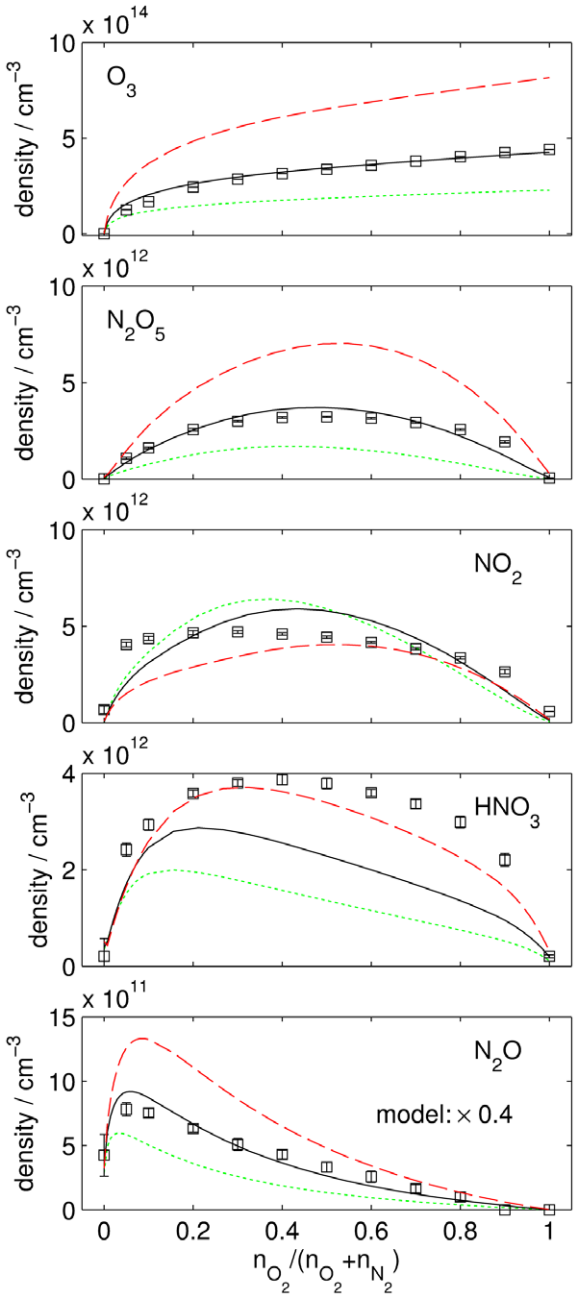

Figure B3. Sensitivity analysis of Ar^* source term magnitude: The black line reproduces the results shown in figure 11. Green dotted line: The magnitude of the argon source term is multiplied by 0.5. Red dashed line: The magnitude of the argon source term is multiplied by 2.

- As more O_3 is produced, NO_2 is converted to N_2O_5 faster than in the basic study.
- For the production of NO the reaction of N with O_2 (R34) becomes more important.
- With rising shielding gas content, the generation of N_2O from N_2^* and O_2 (R26) increases.

B.5. Influence of the feed gas humidity

The densities obtained are shown in figure B5.

- With increasing humidity, less O is available as O is consumed in reactions with HO_2 (R46) and OH (R44).
- If no humidity is available, NO cannot be generated via the main pathway (from N and OH, R64) in the effluent and is generated in the reaction of N and O with a third body (R37), from N_2^* and O with a third body (R86) and from the reaction of N with O_2 (R32).
- If much humidity is available, large amounts of NO_2 and HNO_3 can be expected even when no oxygen is present. It is noted that NO_2, HNO_3 and HNO_2 in the range of some 10^{12} cm^{-3} were indeed detected with pure nitrogen shielding while the system tubes were flushed. However, the humidity was not quantified during this drying phase and therefore the data is not shown.

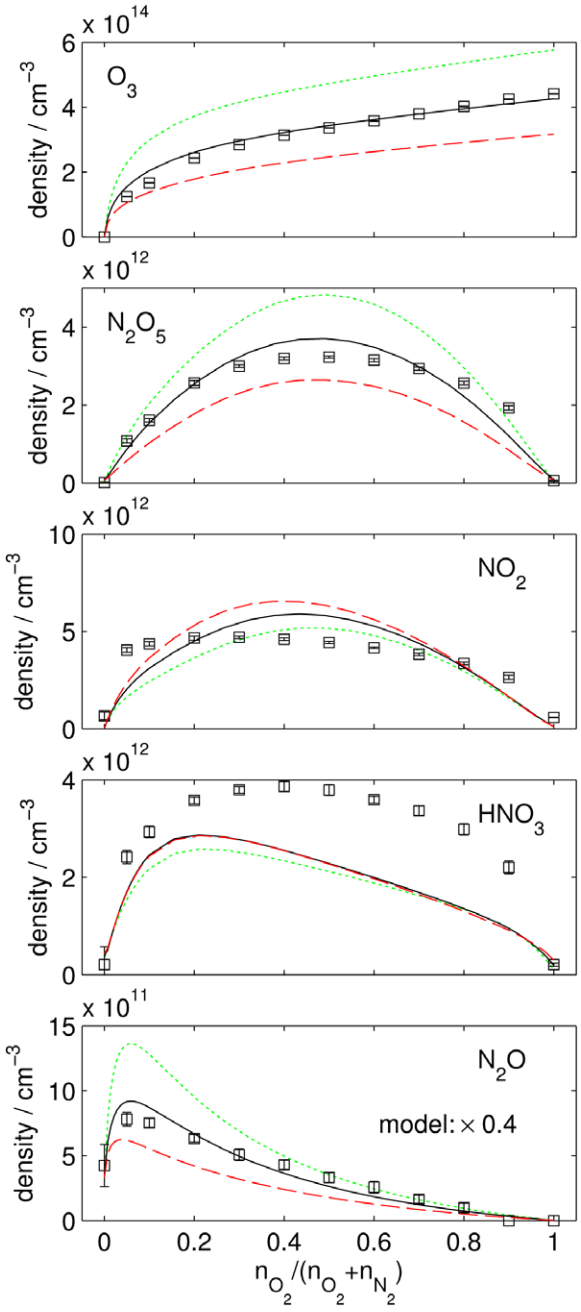

Figure B4. Sensitivity analysis of shielding gas diffusion: The black line reproduces the results shown in figure 11 (maximum shiedling gas density in the plasma plume: 2.4%). Green dotted line: 0.9%. Red dashed line: 6.5%.

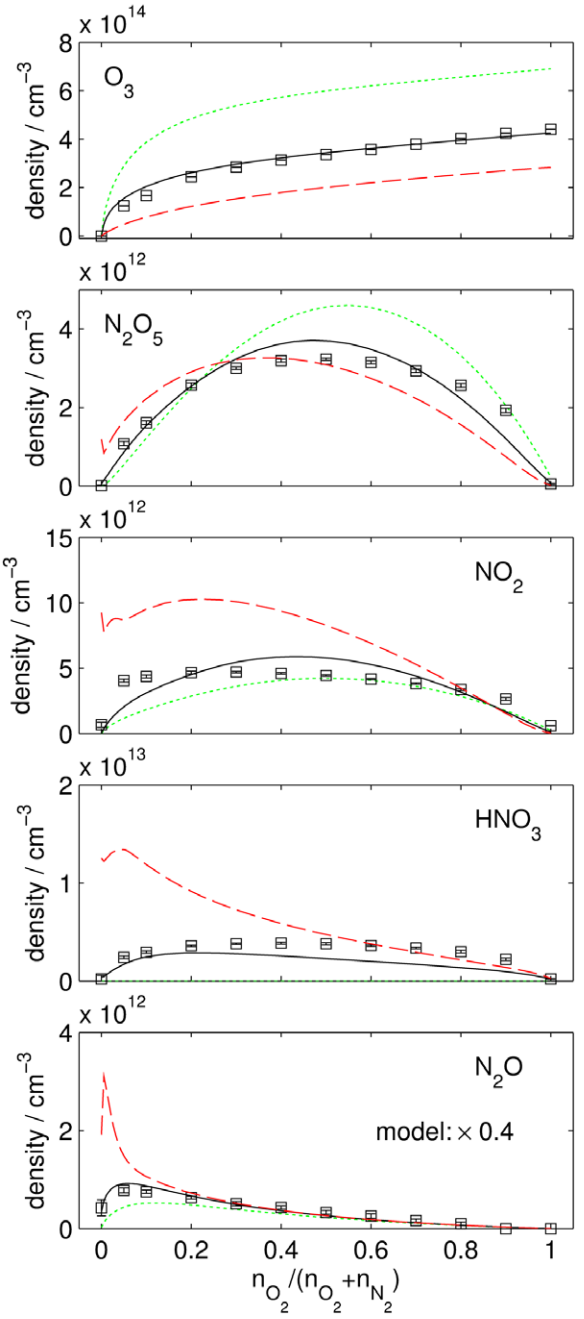

Figure B5. Sensitivity analysis of feed gas humidity: The black line reproduces the results shown in figure 11 (H_2O density: 5 ppm). Green dotted line: 0 ppm. Red dashed line: 50 ppm.

B.6. Influence of the $Ar^*/Ar_2^* + N_2$ *branching ratio*

The densities obtained are shown in figure B6. The same branching rates for quenching of Ar^* and Ar_2^* were assumed.

- The RONS densities are not heavily affected by the branching ratio.
- The underlying mechanisms for the NO generation change: While the generation of NO from N and OH (R64) still produces most, the generation from N_2^* and O_2 (R86) becomes almost as important. This also effects the changes observed in the NO_2, HNO_3 and N_2O_5 density.
- The N_2O density increases with the amount of N_2^* produced as can be expected from reaction R26.

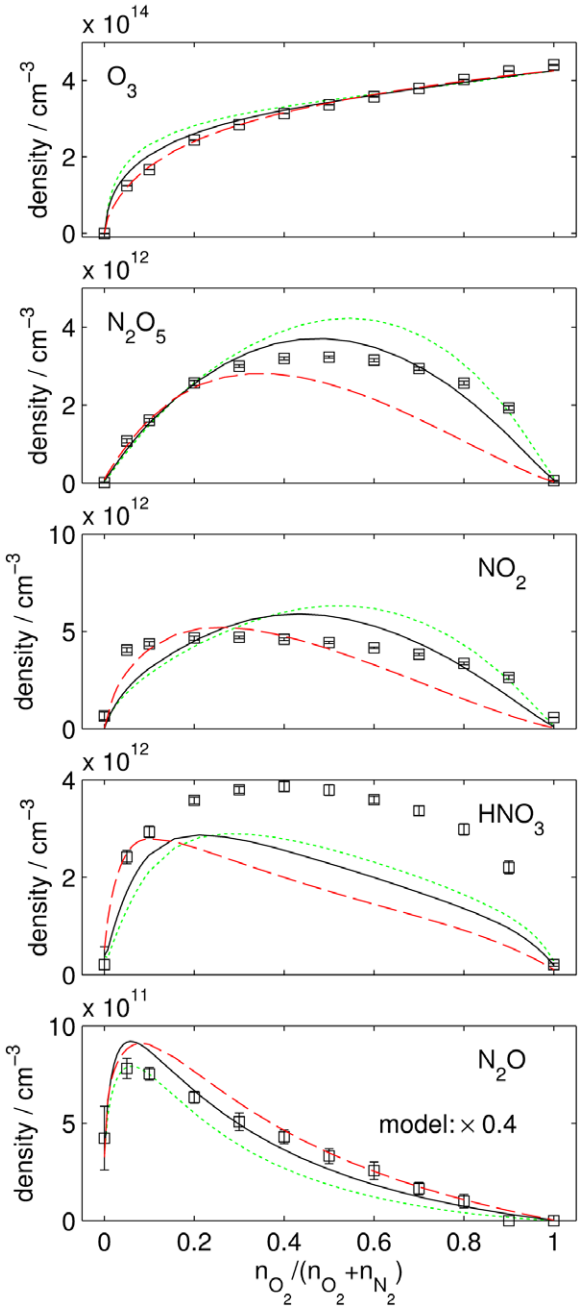

Figure B6. Sensitivity analysis of $Ar^*/Ar_2^* + N_2$ branching ratio: The black line reproduces the results shown in figure 11 (branching ratio 0.5). Green dotted line: Branching ratio 0.2 (more N). Red dashed line: Branching ratio 0.8 (more N_2^*).

References

[1] Kong M G *et al* 2009 Plasma medicine: an introductory review *New J. Phys.* **11** 115012

[2] Fridman A and Friedman G 2012 *Plasma Medicine* (New York: Wiley)

[3] Von Woedtke T, Reuter S, Masur K and Weltmann K D 2013 Plasmas for medicine *Phys. Rep.* **530** 291–320

[4] Graves D B 2014 Low temperature plasma biomedicine: a tutorial review *Phys. Plasmas* **21** 080901–2100

[5] Iza F *et al* 2008 Microplasmas: sources, particle kinetics, and biomedical applications *Plasma Process. Polym.* **5** 322–44

[6] Park G *et al* 2012 Atmospheric-pressure plasma sources for biomedical applications *Plasma Sources Sci. Technol.* **21** 043001

[7] Lu X, Laroussi M and Puech V 2012 On atmospheric-pressure non-equilibrium plasma jets and plasma bullets *Plasma Sources Sci. Technol.* **21** 034005

[8] Ehlbeck J *et al* 2011 Low temperature atmospheric pressure plasma sources for microbial decontamination *J. Phys. D: Appl. Phys.* **44** 013002

[9] Graves D B 2012 The emerging role of reactive oxygen and nitrogen species in redox biology and some implications for plasma applications to medicine and biology *J. Phys. D: Appl. Phys.* **45** 263001

[10] Reuter S *et al* 2012 From RONS to ROS: tailoring plasma jet treatment of skin cells *IEEE Trans. Plasma Sci.* **40** 2986–93

[11] Schmidt-Bleker A, Reuter S and Weltmann K D 2014 Non-dispersive path mapping approximation for the analysis of ambient species diffusion in laminar jets *Phys. Fluids* **26** 083603

[12] Schmidt-Bleker A, Winter J, Iseni S, Dünnbier M, Weltmann K and Reuter S 2014 Reactive species output of a plasma jet with a shielding gas device-combination of FTIR absorption spectroscopy and gas phase modelling *J. Phys. D: Appl. Phys.* **47** 145201

[13] Tresp H, Hammer M U, Weltmann K D and Reuter S 2013 Effects of atmosphere composition and liquid type on plasma-generated reactive species in biologically relevant solutions *Plasma Med.* **3** 45–55

[14] Barton A 2014 *Impact of Non-Thermal Plasma on Cell Signaling in Keratinocytes* (Greifswald: Ernst-Moritz-Arndt-Universität)

[15] Bekeschus S, Iseni S, Reuter S, Masur K and Weltmann K D 2015 Nitrogen shielding of an argon plasma jet and its effects on human immune cells *IEEE Trans. Plasma Sci.* **43** 776–81

[16] Jablonowski H *et al* 2015 Plasma jet's shielding gas impact on bacterial inactivation *Biointerphases* **10** 029506

[17] Pavlovich M J, Clark D S and Graves D B 2014 Quantification of air plasma chemistry for surface disinfection *Plasma Sources Sci. Technol.* **23** 065036

[18] Liu D X, Bruggeman P, Iza F, Rong M Z and Kong M G 2010 Global model of low-temperature atmospheric-pressure He^+ H_2O plasmas *Plasma Sources Sci. Technol.* **19** 025018

[19] Sakiyama Y, Graves D B, Chang H W, Shimizu T and Morfill G E 2012 Plasma chemistry model of surface microdischarge in humid air and dynamics of reactive neutral species *J. Phys. D: Appl. Phys.* **45** 425201

[20] Murakami T, Niemi K, Gans T, O'Connell D and Graham W G 2013 Chemical kinetics and reactive species in atmospheric pressure helium–oxygen plasmas with humid-air impurities *Plasma Sources Sci. Technol.* **22** 015003

[21] Van Gaens W and Bogaerts A 2013 Kinetic modelling for an atmospheric pressure argon plasma jet in humid air *J. Phys. D: Appl. Phys.* **46** 275201

[22] Sakiyama Y and Graves D B 2009 Neutral gas flow and ring-shaped emission profile in non-thermal RF-excited plasma needle discharge at atmospheric pressure *Plasma Sources Sci. Technol.* **18** 025022

[23] Naidis G 2011 Modelling of plasma bullet propagation along a helium jet in ambient air *J. Phys. D: Appl. Phys.* **44** 215203

[24] Breden D, Miki K and Raja L 2012 Self-consistent two-dimensional modeling of cold atmospheric-pressure plasma jets/bullets *Plasma Sources Sci. Technol.* **21** 034011

[25] Boeuf J, Yang L and Pitchford L 2013 Dynamics of a guided streamer ('plasma bullet') in a helium jet in air at atmospheric pressure *J. Phys. D: Appl. Phys.* **46** 015201

[26] Babaeva N Y and Kushner M J 2014 Interaction of multiple atmospheric-pressure micro-plasma jets in small arrays: He/O_2 into humid air *Plasma Sources Sci. Technol.* **23** 015007
[27] Van Gaens W, Iseni S, Schmidt-Bleker A, Weltmann K D, Reuter S and Bogaerts A 2015 Numerical analysis of the effect of nitrogen and oxygen admixtures on the chemistry of an argon plasma jet operating at atmospheric pressure *New J. Phys.* **17** 033003
[28] Naidis G V 2013 Modelling of OH production in cold atmospheric-pressure He–H_2O plasma jets *Plasma Sources Sci. Technol.* **22** 035015
[29] Naidis G 2014 Production of active species in cold helium–air plasma jets *Plasma Sources Sci. Technol.* **23** 065014
[30] Tian W and Kushner M J 2014 Long term effects of multiple DBD pulses on thin liquid layers over tissue: reactive fluences and electric fields *Bulletin of the American Physical Society* vol 59
[31] Lademann J *et al* 2011 Comparison of the antiseptic efficacy of tissue-tolerable plasma and an octenidine hydrochloride-based wound antiseptic on human skin *Skin Pharmacol. Physiol.* **25** 100–6
[32] Metelmann H R *et al* 2012 Experimental recovery of CO_2-laser skin lesions by plasma stimulation *Am. J. Cosmetic Surg.* **29** 52–6
[33] Schmidt A *et al* 2015 Non-thermal plasma activates human keratinocytes by stimulation of antioxidant and phase II pathways *J. Biol. Chem.* **290** 6731–50
[34] Bekeschus S *et al* 2014 Hydrogen peroxide: a central player in physical plasma-induced oxidative stress in human blood cells *Free Radical Res.* **48** 542–9
[35] Daeschlein G *et al* 2014 In vitro susceptibility of multidrug resistant skin and wound pathogens against low temperature atmospheric pressure plasma jet (APPJ) and dielectric barrier discharge plasma (DBD) *Plasma Process. Polym.* **11** 175–83
[36] Iseni S, Schmidt-Bleker A, Winter J, Weltmann K D and Reuter S 2014 Atmospheric pressure streamer follows the turbulent argon air boundary in a MHz argon plasma jet investigated by OH-tracer PLIF spectroscopy *J. Phys. D: Appl. Phys.* **47** 152001
[37] Schmidt-Bleker A, Reuter S and Weltmann K 2015 Quantitative schlieren diagnostics for the determination of ambient species density, gas temperature and calorimetric power of cold atmospheric plasma jets *J. Phys. D: Appl. Phys.* **48** 175202
[38] Reuter S, Schmidt-Bleker A, Iseni S, Winter J and Weltmann K D 2014 On the bullet-streamer dualism *IEEE Trans. Plasma Sci.* **42** 2428–9
[39] Schmidt-Bleker A *et al* 2013 Controlling the effluent chemistry of a CAP jet for biomedical applications: FTIR diagnostics and gas phase modeling *Bulletin of the American Physical Society* vol 58
[40] Dünnbier M *et al* 2013 Ambient air particle transport into the effluent of a cold atmospheric-pressure argon plasma jet investigated by molecular beam mass spectrometry *J. Phys. D: Appl. Phys.* **46** 435203
[41] Van Gaens W, Bruggeman P and Bogaerts A 2014 Numerical analysis of the NO and O generation mechanism in a needle-type plasma jet *New J. Phys.* **16** 063054
[42] Weltmann K D *et al* 2009 Atmospheric pressure plasma jet for medical therapy: plasma parameters and risk estimation *Contrib. Plasma Phys.* **49** 631–40
[43] Reuter S, Winter J, Schmidt-Bleker A, Tresp H, Hammer M U and Weltmann K D 2012 Controlling the ambient air affected reactive species composition in the effluent of an argon plasma jet *IEEE Trans. Plasma Sci.* **40** 2788–94
[44] Bösel A, Ehlbeck J, König N, Salewski K D and Röpcke J 2012 On enhanced tuning capabilities of external cavity lasers using acousto-optic modulators *Opt. Rev.* **19** 332–6
[45] Bösel A and Salewski K D 2009 Fast mode-hop-free acousto-optically tuned laser: theoretical and experimental investigations *Appl. Opt.* **48** 818–26
[46] Schröter S *et al* 2013 Time-resolved characterization of a filamentary argon discharge at atmospheric pressure in a capillary using emission and absorption spectroscopy *J. Phys. D: Appl. Phys.* **46** 464009
[47] Niermann B, Böke M, Sadeghi N and Winter J 2010 Space resolved density measurements of argon and helium metastable atoms in radio-frequency generated He–Ar micro-plasmas *Eur. Phys. J. D: At. Mol. Opt. Plasma Phys.* **60** 489–95
[48] Niermann B, Reuter R, Kuschel T, Benedikt J, Böke M and Winter J 2012 Argon metastable dynamics in a filamentary jet micro-discharge at atmospheric pressure *Plasma Sources Sci. Technol.* **21** 034002
[49] Johnson T J, Sams R L and Sharpe S W 2004 The PNNL quantitative infrared database for gas-phase sensing: a spectral library for environmental, hazmat, and public safety standoff detection *Optical Technologies for Industrial, Environmental, and Biological Sensing. Int. Society for Optics and Photonics* 159–67
[50] Rothman L S *et al* 2004 The HITRAN 2004 molecular spectroscopic database *J. Quant. Spectrosc. Radiat. Transfer* **96** 139–204
[51] Schmidt-Bleker A *et al* 2015 Propagation mechanisms of guided streamers in plasma jets: the influence of electronegativity of the surrounding gas *Plasma Sources Sci. Technol.* **24** 035022
[52] Winter J, Sousa J S, Sadeghi N, Schmidt-Bleker A, Reuter S and Puech V 2015 The spatio-temporal distribution of He (23S1) metastable atoms in a MHz-driven helium plasma jet is influenced by the oxygen/nitrogen ratio of the surrounding atmosphere *Plasma Sources Sci. Technol.* **24** 25015–25
[53] Moravej M, Yang X, Barankin M, Penelon J, Babayan S and Hicks R 2006 Properties of an atmospheric pressure radio-frequency argon and nitrogen plasma *Plasma Sources Sci. Technol.* **15** 204
[54] Van Gessel B, Brandenburg R and Bruggeman P 2013 Electron properties and air mixing in radio frequency driven argon plasma jets at atmospheric pressure *Appl. Phys. Lett.* **103** 064103
[55] Taghizadeh L, Nikiforov A, Morent R, van der Mullen J and Leys C 2014 Determination of the electron temperature of atmospheric pressure argon plasmas by absolute line intensities and a collisional radiative model *Plasma Process. Polym.* **11** 777–86
[56] Schäfer J, Sigeneger F, Foest R, Loffhagen D and Weltmann K D 2010 On plasma parameters of a self-organized plasma jet at atmospheric pressure *Eur. Phys. J. D: At. Mol. Opt. Plasma Phys.* **60** 531–8
[57] Sigeneger F and Loffhagen D 2014 Modeling of striated filaments occurring in a nonthermal RF plasma jet at atmospheric pressure *IEEE Trans. Plasma Sci.* **42** 2498–9
[58] Balcon N, Hagelaar G and Boeuf J 2008 Numerical model of an argon atmospheric pressure RF discharge *IEEE Trans. Plasma Sci.* **36** 2782–7
[59] Lavoie G A, Heywood J B and Keck J C 1970 Experimental and theoretical study of nitric oxide formation in internal combustion engines *Combust. Sci. Technol.* **1** 313–26
[60] Hagelaar G and Pitchford L 2005 Solving the Boltzmann equation to obtain electron transport coefficients and rate coefficients for fluid models *Plasma Sources Sci. Technol.* **14** 722
[61] Puech database 2015 retrieved on January 27, 2015 available from: www.lxcat.net
[62] Biagi-v7 1 database 2015 retrieved on January 27, 2015 available from: www.lxcat.net

[63] Kramida A, Yu R, Reader J and NIST ASD Team 2014 NIST Atomic Spectra Database (version 5.2); available from: http://physics.nist.gov/asd

[64] Keto J W, Hart C F and Kuo C 1981 Electron beam excited mixtures of O_2 in argon. III. Energy transfer to O_2 and O_3 *J. Chem. Phys.* **74** 4450–4

[65] Keto J, Gleason R Jr and Walters G 1974 Production mechanisms and radiative lifetimes of argon and xenon molecules emitting in the ultraviolet *Phys. Rev. Lett.* **33** 1365

[66] Mehnert R, Brede O and Hermann R 1986 Quenching of the argon (4s) levels and of the excimer $Ar_2(^3\Sigma_u^+)$ by N_2,N_2O, SF_6 and CF_3H—a pulse radiolysis study *Int. J. Radiat. Appl. Instrum.: Part C Radiat. Phys. Chem.* **28** 455–60

[67] Millet P, Birot A, Brunet H, Dijolis H, Galy J and Salamero Y 1982 Spectroscopic and kinetic analysis of the VUV emissions of argon and argon-xenon mixtures. I. Study of pure argon *J. Phys. B: At. Mol. Phys.* **15** 2935

[68] PHELPS database 2015 available from: www.lxcat.net

[69] TRINITI database 2015 available from: www.lxcat.net

[70] Morgan database 2015 available from: www.lxcat.net

[71] Piper L G, Velazco J E and Setser D W 1973 Quenching cross sections for electronic energy transfer reactions between metastable argon atoms and noble gases and small molecules *J. Chem. Phys.* **59** 3323–40

[72] Sheldon J W and Muschlitz E E 1978 Quenching cross sections for Ar(3*P*0, 2) and Kr(3*P*0, 2) by H_2O and D_2O *J. Chem. Phys.* **68** 5288–9

[73] Novicki S and Krenos J 1988 Absolute quenching cross section for collisions between Ar (3*P*0, 2) and H_2O *J. Chem. Phys.* **89** 7031–3

[74] Piper L G 1988 State-to-state $N_2(A^3\Sigma_u^+)$ energy-pooling reactions. I. The formation of $N_2(C^3\Pi_u)$ and the Herman infrared system *J. Chem. Phys.* **88** 231–9

[75] Piper L G 1988 $^3\Sigma$-state $N_2(A^3\Sigma_u^+)$ energy pooling reactions. II. The formation and quenching of $N_2(B^3\Pi_g, v' = 1 - 12)$ *J. Chem. Phys.* **88** 6911–21

[76] Dorai R and Kushner M J 2003 A model for plasma modification of polypropylene using atmospheric pressure discharges *J. Phys. D: Appl. Phys.* **36** 666

[77] DeMore W *et al* 1997 JPL publication 97-4 *Evaluation* **12** 1–266

[78] Piper L G 1989 The excitation of $N(^2P)$ by $N_2(A^3\Sigma_u^+, v' = 0, 1)$ *J. Chem. Phys.* **90** 7087–95

[79] Herron J T 1999 Evaluated chemical kinetics data for reactions of N (2*D*), N (2*P*), and $N2(A3\Sigma_u^+)$ in the gas phase *J. Phys. Chem. Ref. Data* **28** 1453–83

[80] Clyne M A and McDermid I S 1975 Mass spectrometric determinations of the rates of elementary reactions of NO and of NO_2 with ground state $N(^4S)$ atoms *J. Chem. Soc. Faraday Trans. 1: Phys. Chem. Condens. Phases* **71** 2189–202

[81] Campbell I and Gray C 1973 Rate constants for O (^3P) recombination and association with N (^4S) *Chem. Phys. Lett.* **18** 607–9

[82] Knipovich O, Rubtsova E and Nekrsov L 1988 Volume recombination of nitrogen atoms in the afterglow of a condensed discharge *Russ. J. Phys. Chem.* **62** 867–70

[83] Tsang W and Herron J T 1991 Chemical kinetic data base for propellant combustion I. Reactions involving NO, NO_2, HNO, HNO_2, HCN and N_2O *J. Phys. Chem. Ref. Data* **20** 609–63

[84] Sehested J, Nielsen O J, Egsgaard H, Larsen N W, Andersen T S and Pedersen T 1998 Kinetic study of the formation of isotopically substituted ozone in argon *J. Geophys. Res.: Atmos.* **103** 3545–52

[85] Atkinson R *et al* 2004 Evaluated kinetic and photochemical data for atmospheric chemistry: volume I-gas phase reactions of O_x, HO_x, NO_x and SO_x species *Atmos. Chem. Phys.* **4** 1461–738

[86] Atkinson R *et al* 1997 Evaluated kinetic and photochemical data for atmospheric chemistry: supplement VI. IUPAC subcommittee on gas kinetic data evaluation for atmospheric chemistry *J. Phys. Chem. Ref. Data* **26** 1329–499

[87] Atkinson R, Baulch D, Cox R, Hampson R Jr, Kerr J and Troe J 1989 Evaluated kinetic and photochemical data for atmospheric chemistry: supplement III. IUPAC subcommittee on gas kinetic data evaluation for atmospheric chemistry *J. Phys. Chem. Ref. Data* **18** 881–1097

[88] Baulch D *et al* 1992 Evaluated kinetic data for combustion modelling *J. Phys. Chem. Ref. Data* **21** 411–734

[89] Cox R and Derwent R 1975 Kinetics of the reaction of HO_2 with nitric oxide and nitrogen dioxide *J. Photochem.* **4** 139–53

[90] National Institute of Standards and Technology 2014 NIST chemical kinetics database available from: http://kinetics.nist.gov/kinetics/index.jsp